Published in final edited form as:
Neuron. 2020 November 25; 108(4): 748–762.e4. doi:10.1016/j.neuron.2020.08.019.

Central vestibular tuning arises from patterned convergence of otolith afferents

Zhikai Liu[1], **Yukiko Kimura**[3], **Shin-ichi Higashijima**[3], **David G. C. Hildebrand**[4], **Joshua L. Morgan**[2], **Martha W. Bagnall**[1,5]

[1]Washington University in St. Louis, Neuroscience, St. Louis, MO,

[2]Washington University in St. Louis, Ophthalmology, St. Louis, MO,

[3]National Institute for Basic Biology, Neurobiology, Okazaki, Japan,

[4]Laboratory of Neural Systems, The Rockefeller University, New York, NY

Abstract

As sensory information moves through the brain, higher-order areas exhibit more complex tuning than lower areas. Though models predict that complexity arises via convergent inputs from neurons with diverse response properties, in most vertebrate systems convergence has only been inferred rather than tested directly. Here we measure sensory computations in zebrafish vestibular neurons across multiple axes *in vivo*. We establish that whole-cell physiological recordings reveal tuning of individual vestibular afferent inputs and their postsynaptic targets. Strong, sparse synaptic inputs can be distinguished by their amplitudes, permitting analysis of afferent convergence *in vivo*. An independent approach, serial-section electron microscopy, supports the inferred connectivity. We find that afferents with similar or differing preferred directions converge on central vestibular neurons, conferring more simple or complex tuning, respectively. Together these results provide a direct, quantifiable demonstration of feedforward input convergence *in vivo*.

eTOC

Though computational models predict how sensory inputs converge in central neurons, it is technically challenging to test these ideas experimentally. With whole-cell recordings in larval zebrafish *in vivo*, Liu et al. demonstrate that the convergence of similarly or differently tuned vestibular afferents produces more simple or complex postsynaptic tuning, respectively.

---

[5]Lead contact: bagnall@wustl.edu.

Author contributions:
Y.K. and S.H. generated the *Tg(nefma:gal4, UAS:GFP)* fish line. Z.L. and M.W.B. conceived the project. Z.L. performed the electrophysiology, confocal imaging experiments and analyzed the data. M.W.B., J.L.M. and D.G.C.H. carried out the serial-section EM imaging and reconstruction. Z.L. and M.W.B. wrote the manuscript with input from all other authors.

Declaration of Interests:
The authors declare no competing interests

Keywords

neural computation; sensory encoding; feedforward excitation; vestibulospinal neuron; electrical synapse; high-pass tuning; sensorimotor transformation; body balance

Introduction

Neurons compute information from many different synaptic inputs. A central challenge in understanding neuronal circuits is determining how the tuning and connectivity of these inputs affect the resulting computations. For example, neurons in visual cortex exhibit simple or complex orientation tuning, which is thought to derive from the convergence of presynaptic inputs with distinct tuning properties (Hubel and Wiesel, 1962, Alonso and Martinez, 1998). Computational models of such input-output relationships have fundamentally shaped the way we think of information processing in the brain (Felleman and Van Essen, 1991, LeCun et al., 2015). However, these models generally require assumptions about many parameters that can only be measured with incompatible approaches: the tuning of the presynaptic population, input connectivity, and synaptic strengths, as well as the activity of the postsynaptic neuron itself. Direct measurements of these parameters simultaneously are prohibitively difficult in most systems, making it hard to define neuronal computations *in vivo*.

Vestibulospinal (VS) brainstem neurons receive direct vestibular sensory inputs from peripheral vestibular afferents (Boyle et al., 1992) and project to the spinal cord (Boyle and Johanson, 2003). Understanding the neuronal computations of VS neurons would not only inform how vestibular sensory signals are processed in the brain, but also provide a mechanistic view of sensorimotor transformation. VS neurons, like other central vestibular neurons, produce diverse responses to head movement. During head tilt or acceleration, some central vestibular neurons exhibit simple cosine-tuned responses, similar to those of the afferents: the strongest activity is evoked by movements in a preferred direction, with little or no response in the orthogonal direction. In contrast, other central vestibular neurons exhibit more complex responses, including bidirectional responses (Peterson, 1970) and spatiotemporally complex tuning (Angelaki et al., 1993). A vectorial model predicts that convergence of several simple cosine-tuned afferents can fully account for the response of either a simple or a complex central vestibular neuron, depending on whether those afferents are similarly tuned or differently tuned (Angelaki, 1992). However, as in other systems, this model has been technically challenging to test experimentally.

We chose to address this question in the larval zebrafish. Vestibular pathways in larval zebrafish are implicated in gaze (Bianco et al., 2012) and postural control (Ehrlich and Schoppik, 2019, Bagnall and Schoppik, 2018), similar to their functions in mammals. The VS neurons in larval zebrafish were also identified as anatomical homologs to those in mammals (Kimmel et al., 1982), indicating that they might share highly conserved functions. Moreover, the VS circuit becomes functional as early as 3 days post-fertilization (dpf) (Mo et al., 2010) in the larval zebrafish, whose small brain is exceptionally accessible for *in vivo* intracellular recordings from identified neurons. Therefore, the larval zebrafish serves as an excellent model organism to investigate how central vestibular neurons compute sensory signals in the vertebrates.

Here we establish a novel approach to record sensory evoked responses *in vivo* from VS neurons in the larval zebrafish. We find that individual afferents evoke large amplitude-invariant excitatory postsynaptic currents (EPSCs), allowing us to separate distinct afferent inputs that converge onto a given VS neuron. This provides a mechanism to simultaneously measure the sensory tuning and synaptic strength of each converging afferent, as well as the response of the postsynaptic neuron. We show that afferents with similar tuning direction preferentially converge, producing simple tuning in the VS neuron. Furthermore, the smaller number of cells with complex bidirectional responses receive input from differently tuned afferents, with consequent simple or complex spiking. We also show that these afferent inputs suffice to predict the tuning of the VS neuron. Together, this work reveals how central neurons in the brain compute sensory information from their presynaptic inputs.

Results:

Sensory evoked responses of vestibulospinal neurons *in vivo*

Traditionally, measurements of neuronal responses to vestibular stimuli have been accomplished by unit recordings (Angelaki and Dickman, 2000, Schor et al., 1984, Fernandez and Goldberg, 1976a). Directly measuring vestibular-evoked synaptic currents in central neurons *in vivo* has been technically challenging (Arenz et al., 2008, Chabrol et al., 2015). We designed a custom whole-cell electrophysiology rig to deliver translational motion stimuli to 4–7 dpf larval zebrafish via an air-bearing motorized sled (Fig. 1A). This setup allows intracellular measurement of sensory-evoked responses from vestibulospinal (VS) neurons over multiple axes *in vivo* for the first time, to the best of our knowledge. To target identified VS neurons, we generated a Tg(nefma:gal4; UAS:GFP) line, whose labelling overlaps dye backfilling from the spinal cord (Figs. 1D, S1), consistent with evidence of *Nefm* expression in mammalian vestibular neurons (Kodama et al., 2020). We recorded spontaneous EPSCs in voltage clamp, at overall rates varying from 1 to 365 EPSC/s. Delivery of translational movement evoked corresponding modulations in EPSC frequency (Fig. 1B and Supplemental Videos S1, S2). The extent of modulation varied depending on the direction of the stimulus delivered across four different directions (Fig. 1C). In this example neuron, EPSC rate was modulated most strongly in the rostral-caudal (R-C) axis and weakly in the dorsal-ventral (D-V) axis, with intermediate strength responses for the diagonal directions (R/D-C/V and R/V-C/D).

Response to translational movement could derive from the vestibular or other sensory inputs. In larval zebrafish, the anterior otolith (utricle) is the sole functional vestibular sensor (Riley and Moorman, 2000). To examine whether utricular signaling is necessary for the observed tuning, we measured the sensory response of VS neurons in the *otog*$^{c.1522+2T>A}$ −/− (*rock solo*) animals, which lack the utricle (Mo et al., 2010, Roberts et al., 2017). Translational stimuli were ineffective at modulating EPSC rate in VS neurons of *rock solo* homozygotes, in contrast to wild-type/heterozygous siblings (representative examples, Fig. 1E). Across all recordings, VS neurons of *rock solo* −/− animals exhibit largely untuned EPSCs compared to siblings, as quantified by a tuning index (Fig. 1F). Thus, this approach reveals sensory-evoked synaptic responses encoding directional vestibular stimuli in identified VS neurons *in vivo*.

Mixed electrical and chemical synapses mediate the transmission from otolith afferents to VS neurons

What properties define the vestibular afferent synapse onto VS neurons? In rodents, vestibular afferent synapses onto vestibulo-ocular reflex neurons exhibit amplitude-invariant synaptic transmission, mediated by specialized vesicular release machinery (Bagnall et al., 2008, McElvain et al., 2015, Turecek et al., 2017). To characterize afferent synaptic input to VS neurons, we electrically stimulated the vestibular (anterior statoacoustic) ganglion while recording from VS neurons in voltage clamp (Fig. 2A). Stimulation evoked a synaptic current with two components. The first component had fast kinetics with short latency (0.56 ± 0.28 ms, n=8), low jitter (0.05 ± 0.04 ms, n=8), and invariant EPSC amplitude (sd/mean: 6.7±3.9%, n=8) across trials. In contrast, the second component had slower kinetics with longer latency (2.3 ± 0.22 ms, n=5) and slightly higher jitter (0.15 ± 0.04 ms, n=5) than the early component, though still consistent with monosynaptic transmission (Wang and McLean, 2014). The second component also exhibited variable amplitudes (sd/mean: 60 ± 37%, n=4) (Fig. 2B). We dissected the two components of evoked EPSCs pharmacologically. Bath application of the gap junction blocker carbenoxolone (CBX, 500 μM) during afferent stimulation substantially reduced the first component of the EPSC, without abolishing the second component (Figs. 2C, E). In contrast, bath application of the AMPA receptor antagonist NBQX (10 μM) abolished the second component of synaptic current (Fig. 2D). Furthermore, the fast EPSCs were not reversed by changing the holding potential (Fig. S2), a signature behavior of electrical synaptic transmission (Akrouh and Kerschensteiner, 2013). Thus, the early and late components of afferent-evoked synaptic currents are mediated by gap junctions and AMPA receptors, respectively. Both EPSC components have low latency and jitter consistent with monosynaptic transmission in larval zebrafish (Wang and McLean, 2014), and abrogating the early component with CBX does not affect the later component, suggesting these two components are mediated by mixed monosynaptic transmission from vestibular afferents to VS neurons. Across VS neurons, the NBQX-sensitive currents accounted for 27.1±20.2% of total charge transfer (n=7, Fig. 2F), demonstrating that gap junctional current is the dominant component mediating synaptic transmission.

To evaluate ultrastructural evidence for mixed synaptic transmission, we re-imaged existing serial ultrathin sections of a 5.5 dpf larval zebrafish (Hildebrand et al., 2017) at sufficiently high resolution (1–4 nm/px) to identify synaptic contacts between myelinated utricular afferents and VS neurons, identified anatomically. We found evidence for electrical transmission between utricular afferent axons and VS neurons in the form of tight junction structures, recognizable by the close apposition between pre- and post-synaptic membranes so that both membranes appear as one (Fig. 2G). Similarly, we identified utricular to VS chemical synapses based on the parallel adjoining membranes and vesicles clustered near a postsynaptic density (Fig. 2H). These data are consistent with anatomical evidence for mixed electrical / chemical transmission at this synapse in adult fish (Korn et al., 1977) and rat (Nagy et al., 2013). Together, these results demonstrate that VS neurons receive vestibular afferent inputs mediated by amplitude-invariant gap junctional (electrical) and variable amplitude glutamatergic (chemical) synapses.

Inferring afferent tuning from distinct EPSCs

Because electrically mediated EPSCs from afferents to VS neurons exhibited a fixed amplitude, we hypothesized that we could distinguish the activity of individual otolith afferents converging onto a given VS neuron by their characteristic EPSC amplitudes. Indeed, spontaneous and sensory-evoked EPSCs recorded in VS neurons often fell into distinctive size bins, as visualized in a histogram of EPSC amplitudes (Figs. 3A, B). EPSCs were sorted into three clusters with unsupervised learning (see Methods), primarily leveraging their amplitudes. Each of these EPSC clusters showed a stereotypical amplitude and waveform in this example neuron (Fig. 3A, inset). To test whether each cluster of EPSCs amplitudes corresponds to an individual afferent, we used an approach derived from spike sorting: temporal autocorrelation to test for refractory periods within EPSC event times. Physiologically, one afferent cannot generate two action potentials within its refractory period (Fernandez et al., 1972); thus the EPSCs elicited by that afferent should exhibit a refractory period. The auto-correlogram of EPSCs showed the average activity of other EPSCs relative to the timepoint of the reference EPSC anchored at 0 ms (Fig. 3C). In this example neuron, an auto-correlogram of all EPSC event times did not show any structure around 0 ms (Fig. 3C, top). In contrast, an auto-correlogram within each EPSC cluster exhibited a gap in event intervals around 0 ms, suggesting a clear refractory period (Fig. 3C, bottom). This result was not due to limitations in event identification at brief intervals, because the fast kinetics of these EPSCs allowed us to distinguish events as close together as 0.2 ms, as seen in the all-event autocorrelogram (top), and this is much shorter than the typical refractory period (see Methods). Furthermore, cross-correlograms between EPSC clusters did not show this structure, consistent with the notion that they arise from independent inputs (Fig. S3). Accordingly, we can interpret these three EPSC clusters as deriving from the activity of three distinct presynaptic afferents (Fig. 3D, left). Because of the high fidelity of electrical transmission, each EPSC cluster effectively reads out the spiking of an individual afferent, allowing us to measure presynaptic activity via postsynaptic recording (Fig. 3D, right).

To test this interpretation of electrophysiological data with a completely independent approach, we reconstructed the whole volume of myelinated utricular inputs onto 11 VS neurons from a high-resolution re-imaged serial-section electron microscopy (EM) dataset acquired from the right side of one 5.5 dpf larval zebrafish (Fig. 4A, B). We found that the connection between myelinated utricular afferents and VS neurons was relatively sparse. All VS neurons were contacted by at least two utricular afferents, but some afferents did not innervate any VS neurons (Fig. 4C). These reconstructions showed that a range of 2–6 afferents (mean±std: 3.4±1.4) converged onto each VS neuron (Fig. 4D). We compared these numbers to those derived from whole-cell physiology, where we inferred the number of convergent afferents from the number of EPSC clusters. Across all VS neuron recordings, we found a range of 0–5 afferents (1.7±1.3) converged onto each VS neuron (Fig. 4E). The smaller number of afferents deduced from physiological recordings is likely because small-amplitude EPSCs were often not successfully clustered, or did exhibit refractory-period structure in autocorrelogram, suggesting they are elicited by multiple sources. Nonetheless, the result from anatomical reconstruction is largely consistent with the overall distribution of afferent contacts as measured by whole-cell physiology. Therefore, these results demonstrate that synaptic inputs from individual vestibular afferents can be separated by their stereotypic EPSC waveforms, yielding inferred afferent convergence consistent with high-resolution anatomical connectivity.

Spatial tuning of inferred otolith afferents

By recording from one VS neuron, we can infer the activity of its presynaptic afferents. This approach thus offers a unique opportunity to measure the sensory tuning of several convergent afferents simultaneously. To determine the spatial tuning of convergent afferent inputs, we delivered 2 Hz, ±0.02 g sinusoidal translational stimuli on four directions in the horizontal plane and recorded the sensory-evoked EPSCs, as shown for an example VS neuron (Fig. 5A). In this example neuron, the inferred utricular afferent (EPSC cluster) with the largest synaptic amplitude responded best to caudally directed acceleration, while two others responded with varying sensitivities to rostrally directed acceleration. All cells had phase leads relative to peak acceleration (Fig. 5B). With these measurements, we can derive the preferred tuning direction, gain and phase of each afferent, as represented by the direction and length of a vector (Fig. 5B, right). To validate the consistency of the vectorial representation, we used a previously established approach (Schor et al., 1984) to quantify the tuning vectors with separately measured responses to two circular stimuli (Fig. S4 B), which showed similar preferred directions as those measured by translational stimuli (Figs. S4 A–C). Across all recordings with the animal oriented side-up, tuning of afferents was strong in the rostral (30/69) and caudal (31/69) directions, but relatively weak in the dorsal (4/69) and ventral (4/69) directions, as represented by an overlay of all inferred afferent tuning vectors (Fig. 5C). When fish were oriented dorsal-up, the axes tested were rostral-caudal and ipsilateral-contralateral (motion along an axis from one ear to the other; ipsilateral indicates acceleration towards the side where the recorded neuron is located). In this position, most afferents were strongly tuned to acceleration towards the contralateral direction (31/60), some exhibited preferential tuning to the acceleration to the rostral (4/60) and caudal (20/60) directions, and only 5/60 afferents were tuned to the ipsilateral direction (Fig. 5D). The decrease in proportion of afferents responsive to rostral translation as compared measured in the side-lying recording is likely due to the suppression of hair cells in the side-lying animal, which may have caused fewer afferents to be active. Overall, these results showed that each afferent in the larval zebrafish exhibits selective responses to different translational stimuli. Afferents overall responded best to acceleration towards the contralateral, rostral, and caudal directions, which correspond to ipsilateral, nose-up and nose-down tilts in postural change (Angelaki and Cullen, 2008), consistent with the distribution of hair cell polarity in the utricular macula (Haddon et al., 1999).

Temporal tuning of inferred otolith afferents

The sensitivity and phase of vestibular afferents varies for motion at different frequencies (Fernandez and Goldberg, 1976b). The otolith afferents ranges from typically more jerk-tuned (tuned to the derivative of acceleration) at low frequencies to more acceleration-tuned at high frequencies. What temporal tuning profile do afferents in larval zebrafish exhibit? We applied translational stimuli with different frequencies (0.5–8 Hz, ±0.02 g) on the R-C axis. In one example neuron, all three inferred otolith afferents showed similar tuning, with progressively stronger responses to increasing frequencies of stimulation (Fig. 6A). Across group data, the average tuning gain in response to stimuli from 0.5 Hz to 8 Hz increased 3.3-fold (measured with stimulus amplitude 0.02 g) or 2.3-fold (measured at 0.06 g) (Fig. 6B). Most afferents (39/48) showed at least a 2-fold increase from 0.5 Hz to 4 Hz in tuning gain at either 0.02 g or 0.06 g. Only one afferent had relatively flat gain (< 50% increase) at both 0.02 g and 0.06 g, and its tuning was overall weak (mean gain: 1.88 and 2.24 EPSC/s respectively), suggesting it was less sensitive or not tuned on the R-C axis. Regardless of tuning direction (rostral: 44%, 21/48; caudal: 56%, 27/48), afferents exhibited a phase lead relative to peak acceleration at various tested stimulus magnitudes and frequencies (Fig. 6C, S5A). On average, the phase lead at low frequency (0.5 Hz) was 84.0° for 0.02 g and 78.6° for 0.06 g. In other words, the peak response was almost 90° prior to peak acceleration, and therefore best described as encoding jerk at low frequencies. At high frequency (8 Hz), the phase lead was reduced to 33.6° for 0.02 g and 39.3° for 0.06 g, partway between the peaks of jerk and acceleration. The temporal dynamics of the afferents resembled those of previously reported irregular units (Goldberg et al., 1990), with low spontaneous firing rates (10.28±9.1 EPSC/s) and larger coefficients of variation (CV). The average CV across inferred afferents was 0.97±0.24, and the smallest CV was 0.5 (Fig. S5B), indicating that no regular-firing otolith afferents were detected synapsing onto VS neurons. We conclude that the otolith afferents act as a high-pass filter, encoding a mixture of acceleration and jerk, similar to irregular otolith afferents in primates (Laurens et al., 2017, Jamali et al., 2013).

Preferential convergence

Individual VS neurons can receive inputs from afferents with similar (Fig. 6A) or different tuning (Fig. 5B). Is afferent tuning convergence random or structured? To answer this question, we compared the sensory responses of inferred afferents to 0.02 g, 2 Hz translational stimuli, using their tuning vectors quantified in the analysis of preferred spatial directions (Fig. 7A). The angle between the vectors indicates the similarity of convergent inputs, with a small angle (<45°) for a VS neuron with similarly tuned inputs and a large angle (>135°) for a VS neuron with differently tuned inputs. From 43 VS neurons recorded in the side-up orientation, 60% (38/63) of converging afferent pairs had small angles and 27% (17/63) had large angles. Compared to a random pairing angle distribution generated by bootstrapping, the percentage of similarly tuned convergent afferent pairs was significantly higher than chance (Fig. 7B, left). From 36 VS neurons recorded in the dorsal-up orientation, there were 71% (37/52) of inferred converging afferent pairs with small angles, and only 2% (1/52) with large angles due to the small number of ipsilaterally tuned afferents (Fig. 5D). Nonetheless, the probability of similarly tuned afferent convergence for small converging angles was significantly higher than chance (Fig. 7B, right). For afferent pairs with a large converging angle (45°-90°, 90°-135°, 135°-180°), their probabilities were slightly lower than the respective estimated distributions by bootstrapping. Accordingly, along a given body axis (R-C or I-C), convergent afferents are also more likely to encode similar tuning directions (Fig. 7C). These results suggest that afferents with similar tuning direction preferentially converge at rates exceeding what would be expected by random connectivity.

Do converging afferents also have similar tuning phase regardless of their tuning direction? Most afferents are phase-leading with 2 Hz, 0.02 g stimulation (Figs. 6 and 7D, inset), and the phase difference between afferents is small (R-C: 41° ±16°, n=177, I-C: 33° ±17, n=60). Consequently, most afferent pairs (R-C: 68 ±4.6%; I-C: 68 8%) selected randomly have very small phase difference (phase diff. < 22.5°) (Fig. 7D). Both the probability of converging afferents having similar phase (phase diff. < 22.5°) (R-C, 73%, 75/103; I-C, 59%, 20/34) and the cumulative distribution (Fig. S6) lay within the bootstrap predications on the R-C and I-C axes. Therefore, tuning phase between converging afferent pairs is similar, in accordance with their relatively homogeneous distribution.

In conclusion, we found that afferents forming synaptic connections with the same postsynaptic VS partner typically have similar spatial tuning properties. In particular, afferents with similar tuning direction preferentially converge, which may explain the long-standing observation that most VS neurons exhibit simple cosine tuning (Peterson, 1970, Schor et al., 1984). However, a non-negligible number of VS neurons receive convergent input from differently tuned afferents, providing a potential source for the complex spatiotemporal tuning of central vestibular neurons.

Complex central tuning arises from divergent afferent inputs

Complex sensory tuning of central neurons is thought to arise from convergence of more simply tuned inputs with differing spatial and temporal properties in vestibular (Angelaki et al., 1993), visual (Jia et al., 2010), and somatosensory (Petersen, 2007, Roy et al., 2011) systems. For example, complex tuning such as bidirectional (Peterson, 1970) and broadly tuned sensory responses (Angelaki, 1992) of central vestibular neurons can be computationally reconstructed from multiple modelled cosine-tuned inputs. However, directly measuring these inputs has been technically difficult, and it is unclear whether such models can sufficiently explain the activity of central neurons. Therefore, we took advantage of the inferred afferent spiking to examine whether the tuning of VS neurons can be constructed from the convergence of otolith afferents.

During sensory stimulation, most VS neurons showed simple membrane potential responses to translational stimuli, with depolarization or spiking during only one phase of acceleration (Fig. 8A, top, and Supplemental Video S3). In contrast, some VS neurons exhibited multiple depolarized periods during each stimulation cycle, resulting in a complex response. In both subthreshold and spiking VS neurons depolarization or spiking exhibited two peaks per stimulus cycle (Fig. 8A, bottom). To examine how spiking responses are generated from afferent inputs, we measured the EPSC tuning in the same VS neurons. In the VS neuron with simple spiking responses (raster, top), sensory evoked EPSCs exhibit three distinct amplitudes (Fig. 8B, top), indicating that three afferents converge onto the cell. These three afferents showed similar tuning to each other, with the strongest responses for rostrally directed acceleration, consistent with the simple spike tuning. In contrast, the four inferred afferents that converge onto an example complex cell exhibited a different tuning pattern (Fig. 8B, bottom). Two afferents were tuned to rostrally directed acceleration and the other two to caudally directed acceleration, consistent with the bidirectional spike tuning. Some VS neurons (37/71) did not spike spontaneously or during the largest sensory stimulation we could deliver while holding the cell. Therefore, we injected a small bias current to evoke spiking in a subset of VS neurons (15/27, see Methods). Membrane potential was shifted by the bias current but its relationship to sensory stimulation was largely unaffected by this manipulation (Fig. S8A), though this may not be the same response as would be seen with larger sensory stimuli. Both unidirectional and bidirectional responses were observed in VS neurons, regardless of whether they were exhibiting spontaneous or current-induced spiking. To investigate the relationship between convergent afferent tuning and VS responses, we ranked the spiking responses of VS neurons based on the similarity of EPSC inputs. The similarity index ranges from 0–1, with smaller values representing more divergent EPSC input tuning and larger value representing more similar tuning (see Methods). The spiking responses of all VS neurons is represented in a heatmap in Fig. 8C, with cells ordered from most similar tuning to least similar tuning. The example cells shown in Fig. 8B have input similarity indices of 0.45 and 0.12, respectively (Fig. 8C, red asterisks). VS neurons with more similar EPSC inputs (Fig. 8C, top) typically have more simple postsynaptic spiking responses, with action potentials occurring in just one phase of the stimulus cycle. In contrast, VS neurons with more divergent EPSC inputs (Fig. 8C, bottom) show more complex postsynaptic spiking responses, with action potentials at two phases of the stimulus cycle.

To quantify this relationship across the population, we compared the afferent inputs similarity with the tuning complexity of each VS neuron. The inputs similarity index is defined by the phase of afferent inputs and their EPSC amplitudes, and the tuning complexity index used the original classifier developed in visual cortical neurons to quantify the complexity of the postsynaptic neuron’s membrane potential or spiking responses (Skottun et al., 1991). In this metric, neurons with simple tuning show large AC and small DC spiking responses, whereas cells with more complex (multi-phasic) activity exhibit small AC and large DC spiking responses. We found that for both subthreshold (Fig. 8D) and spike (Fig. 8E) tuning, the AC/DC ratio was positively correlated with the similarity index of afferent inputs. In other words, convergence of more similarly tuned afferents yields a more simple postsynaptic tuning, and the convergence of more differently tuned afferents generates a more complex postsynaptic tuning. Thus, the properties of converging afferents are directly linked to postsynaptic tuning, with bidirectionally sensitive neurons derived from summation of oppositely tuned inputs. These bidirectionally sensitive neurons were only seen for the R-C axis, not the I-C axis (Fig. 8F), though similar bidirectional “delta” type neurons have been found in multiple axes in cats (Peterson 1970).

Discussion

Sensory convergence in the central vestibular nuclei

Taking advantage of the invariant synaptic transmission of electrical synapses, we separated distinct afferent inputs that converge onto VS neurons and measured the spatial and temporal tuning of each converging afferent *in vivo*. This analysis is facilitated by the sparseness of connectivity, with < 6 afferents synapsing with each VS neuron. Our data reveal that sparse but powerful afferent synaptic contacts, located on the lateral dendrites of VS neurons, are sufficient to drive the membrane potential of the cell during sensory stimulation. These data are consistent with observations in the mammalian literature: anatomically, very few otolith afferent terminals are observed in the lateral vestibular nucleus (Newlands and Perachio, 2003), but physiologically, afferent stimulation elicits monosynaptic EPSPs in VS neurons (Boyle et al., 1992). Although these large afferent inputs drive sensory responses, VS neurons receive a wealth of non-vestibular synaptic contacts on their large dendritic arbors. This is in line with previous findings that the activity of VS neurons is regulated by locomotion (Orlovsky, 1972), proprioception (Neuhuber and Zenker, 1989), and other inputs (Sarkisian, 2000, Witts and Murray, 2019). Interestingly, lateral geniculate neurons (LGN) of the visual thalamus display a similar pattern of connectivity, with sparse, powerful afferent inputs from retinal ganglion cells and weaker, diverse inputs from other sources (Usrey et al., 1999, Sherman, 2005). Moreover, granule cells in cerebellum also receive sparse mossy fiber inputs, and their synaptic inputs exhibit pathway-specific biophysical properties (Chabrol et al., 2015). Our findings suggest that this configuration is common to VS neurons as well.

Similarly tuned otolith afferents preferentially converge onto VS neurons (Fig. 7), demonstrating that feedforward excitation can generate central neurons with simple response properties. In a similar vein, thalamocortical inputs with similar angular tuning also preferentially project onto the same site in somatosensory cortex, and the preferred tuning direction of a given cortical neuron can be predicted by that of the presynaptic thalamic neuron (Bruno et al., 2003). Furthermore, we found that convergence of differently tuned afferents can yield a more complex postsynaptic response in central vestibular neurons, similar to bidirectional or complex tuning observed previously in cats (Peterson, 1970) and primates (Angelaki and Dickman, 2000). This result generally supports the hypothesized model (Angelaki, 1992) that the tuning of central vestibular neurons can be constructed from cosine-tuned inputs with varying spatiotemporal properties. However, we find that convergence of differently tuned afferents can also yield simple tuning in VS neurons (cells in upper left, Fig. 8E), suggesting other factors such as inhibition (Straka and Dieringer, 1996) and thresholding (Priebe et al., 2004) might be involved. We found no evidence for polysynaptic excitatory circuits during afferent stimulation (Fig. S7 A and B), and modelling indicates that excitatory synaptic input is sufficient to predict subthreshold membrane potential and tuning (Fig. S7 C–F). However, stronger stimuli might elicit inhibition and other nonlinearities. Across brain regions, sensory tuning of central neurons is constructed by a variety of mechanisms. These include afferent convergence patterns (Alonso and Martinez, 1998, Priebe and Ferster, 2012), local excitatory or inhibitory modulation (Wilent and Contreras, 2005), and nonlinear dendritic computations (Lavzin et al., 2012). Our results demonstrate that the sensory response of a central neuron can be constructed from its afferent inputs in a direct feedforward manner.

Otolith afferent tuning properties in the larval zebrafish

The derived spatial tuning profile of afferents in the larval zebrafish is similar to the polarity of the hair cells in otolith macula, consistent with results in fish (Fay, 1984, Platt, 1977) and primates (Fernandez et al., 1972). Notably, tuning to dorsal or ventral acceleration was relatively weak for most afferents, presumably due to the horizontal orientation of the utricular membrane in the larval zebrafish inner ear. Afferents were preferentially tuned to contralateral acceleration (ipsilateral tilt) along the roll axis, consistent with the dearth of ipsilaterally tuned hair cells in larval zebrafish (Haddon et al., 1999). Thus, the absence of bidirectionally tuned neurons in the I-C axis might simply be due to the relative rarity of ipsilaterally tuned hair cells. However, it may also be related to behavioral control: fish make deliberate changes in the pitch axis to change their elevation, but not in the roll axis (Ehrlich and Schoppik, 2017) (Fig. 8F). In species with a more centrally located line of polarity reversal (Fernandez and Goldberg, 1976a, Tomko et al., 1981), we would predict more convergence of oppositely tuned afferents, and correspondingly more complex responses of VS neurons in the roll axis, as seen in cats (Peterson, 1970).

A significant question in vestibular systems is whether central vestibular neurons receive selective projections from afferents with regular as opposed to irregular firing. Both regular and irregular afferents are thought to converge on VS and vestibulo-ocular reflex neurons in mammals, based on studies comparing recruitment thresholds of afferent inputs (Boyle et al., 1992). Our data provide direct evidence that vestibular inputs to VS neurons exhibit classic characteristics of irregular afferents (Eatock and Songer, 2011): high-pass tuning, low spontaneous firing rate, and high CV of firing (Fig. S5A–C). It is unknown whether regular utricular afferents exist in the larval zebrafish. Although regular utricular afferents were observed in guitarfish (Budelli and Macadar, 1979), they appear absent in toadfish (Maruska and Mensinger, 2015) and sleeper goby (Lu et al., 2004). Based on serial-section EM reconstructions, many afferents make no contacts with VS neurons (Fig. 4C), leading us to conclude that either regular afferents have not yet developed or that they do not contact VS neurons in the larval zebrafish.

Linear and fast synaptic transmission via gap junctions

Our data reveal that electrical synapses mediate linear synaptic transmission from otolith afferents to VS neurons. Although electrical transmission is implicated in the formation of neural circuits during development (Pereda, 2016), other sensory afferent transmission in larval zebrafish, such as at retinotectal synapses, is mediated solely by glutamate (Smear et al., 2007). This suggests that the electrical synapses we identified from vestibular afferents are perhaps not simply a feature of early larval development but play an important role in circuit computations, potentially via their amplitude-invariant transmission. Interestingly, mammalian vestibular afferent synapses also exhibit amplitude-invariant transmission in the medial vestibular nucleus (Bagnall et al., 2008) and cerebellum (Arenz et al., 2008, Chabrol et al., 2015), but via specialized glutamatergic terminals (Turecek et al., 2017, McElvain et al., 2015), indicating that frequency-independent transmission is a hallmark of vestibular signaling across vertebrates. Furthermore, mixed electrical and chemical synapses have been anatomically identified between vestibular afferents and VS neurons in both adult fish (Korn et al., 1977) and rodents (Nagy et al., 2013), suggesting the mixed synapse may be a conserved mechanism across species to implement fast, frequency-independent transmission in the lateral vestibular nucleus. The amplitude invariance of this connection allowed us to examine whether there was any relationship between an afferent’s sensory gain or firing rate and the synaptic amplitude it evokes in a VS neuron. No correlation appeared in either of these measures (Fig. S5D, E), indicating that at least within this population, weaker synaptic strength is not compensated for by higher firing rates.

VS pathway underlying sensorimotor transformation

The VS pathway is important for posture control. Larval zebrafish swim at high frequencies up to 100 Hz (McLean and Fetcho, 2009) and are naturally unstable in water (Ehrlich and Schoppik, 2017). Our study examined the response of VS neurons with translational stimuli in the range of 0.04–0.12 g and 0.5–8 Hz, head movement parameters comparable to slow swimming (Voesenek et al., 2016) or small angle tilting motion in the larval zebrafish. In the roll axis all VS neurons are tuned to ipsilateral tilt (Fig. S8B), consistent with data from calcium imaging (Migault et al., 2018, Favre-Bulle et al., 2018), suggesting they might excite specific motor units in the spinal cord to produce compensatory movements (Bagnall and McLean, 2014). On the pitch axis, VS neurons have more heterogeneous responses, including simple tuning to either rostral or caudal acceleration (Fig. S8B), as well as complex responses (Fig. 8) to both directions. Thus, when the animal is destabilized by excessive nose-up or nose-down tilts, VS neurons might activate non-specific motor units, increasing the likelihood of swim bouts to regain balance (Ehrlich and Schoppik, 2017).

The high-pass tuning and phase lead of otolith afferents innervating VS neurons will make larvae most sensitive to ongoing changes in tilt or acceleration, especially at high frequency. These data are consistent with behavioral observations that larvae become more likely to swim to correct their position in the pitch axis when angular velocity (i.e., changing tilt) reaches a critical threshold (Ehrlich and Schoppik, 2017). This compensatory postural adjustment, which relies on both trunk and fins, is absent in *rock solo* larvae (Ehrlich and Schoppik, 2019), in line with our results on the absence of sensory tuning in those animals. Larval VS neurons receive similar amounts of inputs from rostrally and caudally tuned afferents, suggesting both nose-up and nose-down tilts are equally detected by the VS pathway. In contrast, the vestibulo-ocular pathway shows an anatomical bias for representation of nose-up body tilt (Schoppik et al., 2017). This bias indicates that different strategies might be involved to adjust body posture and eye position for pitch movements in larval zebrafish.

Moreover, it is important for animals to distinguish self-generated and external vestibular signals. We described the direct excitatory inputs from vestibular afferents onto the VS neurons during passive movements. How do self-generated motion signals modulate the activities of VS neurons? In the related lateral line system, locomotor signals inhibit afferent activity via brainstem efferents that preferentially suppress hair cells encoding posterior-directed deflections, which would occur during normal swim (Lunsford et al., 2019, Pichler and Lagnado, 2020). In contrast, in the mammalian vestibular system, afferent activity appears normal during self-generated movement but central VS neurons show reduced responses, likely due to inhibition from cerebellar Purkinje cells (Cullen, 2019). In the future, it would be interesting to use *in vivo* whole-cell physiology to investigate how central vestibular neurons distinguish self-generated movements from passive movements in the larval zebrafish.

STAR methods

Resource availability

Lead contact: Further information and requests for resources and reagents should be directed to and will be fulfilled by the Lead Contact, Martha Bagnall (bagnall@wustl.edu).

Materials Availability—The fish line generated in this study have been deposited to ZFIN: Tg(nefma:gal4; uas:GFP), ZFIN ID: ZDB-ALT-200623–2

Aligned EM images are available at the following site: http://zebrafish.link/hildebrand16/data/vestibular_right

Data and Code Availability—MATLAB code for analysis is available on https://github.com/bagnall-lab/VStuning_project

EXPERIMENTAL MODEL AND SUBJECT DETAILS

All fish used for experiments were at larval stage from 4–7 dpf before the onset of sexual maturation. The age of the animals used is described in the Method details and/or indicated in the figures. All experiments and procedures were approved by the Animal Studies Committee at Washington University and adhere to NIH guidelines.

Animals were raised and maintained in the Washington University Zebrafish Facility at 28.5°C with a 14:10 light:dark cycle. Larval zebrafish (4–7 dpf) were housed either in petri dishes or shallow tank with system water. Adult animals were maintained up to 1 year old with standard procedure.

Tg(nefma:LRL:Gal4) was established by injecting the construct containing hsp70 promoter (Kimura et al., 2014), and the insertion site was set at the upstream of the nefma gene with the CRISPR target sequence: CATCGACGGATCAATGG. The *Tg(nefma:gal4)* fish line was generated by crossing *Tg(nefma:LRL:Gal4)* with a ubiquitous-Cre fish. The $otog^{c.1522+2T>A}$ −/− (rock solo) mutant is vestibular deficient due to a splice site mutation in *otogelin* (Mo et al., 2010, Roberts et al., 2017). Rock solo homozygotes on a *Tg(nefma:gal4, UAS:GFP)* background were crossed to rock solo WT/heterozygotes to produce clutches containing WT, heterozygotes and homozygotes for recording purposes. The rock solo homozygotes were identified by the absence of anterior otolith (utricle).

Method details:

Electrophysiology: VS neurons were targeted for whole-cell patch clamp recordings based on their characteristic position and fluorescence in the *Tg(nefma:gal4, UAS:GFP)* fish. The larvae (4–7 dpf) were paralyzed by 0.1% α-bungarotoxin and embedded in a 10 mm FluoroDish (WPI) with low-melting point agarose (Camplex SeaPlaque Agarose, 2.4% in system water). Fish were immersed in extracellular solution ([in mM] NaCl 134, KCl 2.9, $MgCl_2$ 1.2, HEPES 10, glucose 10, $CaCl_2$ 2.1, osmolarity ~295 mOsm and pH ~7.5) and a small piece of skin above the brainstem was carefully removed by sharpened tungsten pins. The fish was transferred to an epifluorescence microscope equipped with immersion objectives (Olympus, 40x, 0.8 NA), infrared differential interference contrast optics and air-bearing sled recording table.

Patch pipettes (7–9 MΩ) were filled with internal solution ([in mM] K gluconate 125, $MgCl_2$ 2.5, HEPES 10, EGTA 10, Na_2ATP 4, Alexa Fluor 568 or 647 hydrazide 0.05–0.1, osmolarity ~295 mOsm and pH ~ 7.5). After whole-cell configuration was achieved, voltage clamp and current clamp signals were recorded at room temperature with a Multiclamp 700B, filtered at 10 kHz (current clamp) or 2 kHz (voltage clamp), digitized at 50 kHz with Digidata 1440 (Axon Instruments), and acquired by Clampex 10 (Molecular Devices).

I-V curve measurement: CsMeO4 internal solution ([in mM] CsMeSO3 122, QX314-Cl 1, TEA-Cl 1, MgCl2 3, HEPES 10, EGTA 10, Na2-ATP 4) was used to measure the reversal potential of evoked EPSCs. In the voltage clamp mode, evoked EPSCs at different holding membrane potential (−80–40 mV) were recorded. The amplitude and sign change of EPSCs were determined to plot the I-V curve. Liquid junctional potential was calculated to adjust the measured potential.

Before the vestibular stimulus was delivered to the fish, the immersion objective was removed from the recording chamber. During the recording, series resistance was monitored every 15 s to ensure good recording quality; neurons with series resistance variation > 25% were discarded. After recording, the recorded cell was imaged with epifluorescence to confirm cell identity.

Vestibular stimulation: The recording rig was custom-designed to allow delivering user-controlled movement to the fish during recording without losing whole-cell access. The microscope and a one-axis or two-axis air-bearing sled (Aerotech, ABL1500WB or ABL1500&1500WB) were fixed on an air table. Manipulators (Microstar) and recording platform (ThorLab) were positioned on the sled. The sled was powered with the Aerotech transformers (TM5), NPdrivers (NDRIVECP10-MXU&NDRIVECP20-MXU) and nitrogen gas (Airgas, NI UHP300). Stimuli were designed in Matlab and imported into the program by Aerotech software (Motion Designer/Composer), with additional tuning as required to compensate for the motion of the underlying air table. Movement was recorded by an accelerometer (Sparkfun, ADXL335) attached to the platform. Motion signals were digitized at 50 kHz with Digidata 1440 (Axon Instruments), and acquired in Clampex 10 (Molecular Devices).

Fish were embedded either dorsal side up (movements on rostral-caudal and ipsilateral-contralateral axes) or left/right side up (movements on dorsal-ventral and rostral-caudal axes) and a series of frequency-varying sinusoidal translational stimulus was applied. The stimulus amplitude was set at 0.02 g or 0.06 g (min to max: 0.04 g or 0.12 g respectively), and stimulus frequency range was 0.5–8 Hz. For spatial tuning measurements, linear translation was applied on four different axes (0–180°, 45°-225°, 90°-270°, 135°-315°) on the horizontal plane. Because the two-axis sled was mounted atop a standard electrophysiology air table, there was a slight damping effect during stimulation, most noticeably at the beginning of a sinusoidal waveform. We delivered an adapted stimulus waveform to compensate for this damping effect. Across four translation stimuli, the measured stimulus from the accelerometer showed the acceleration amplitude was 0.0208 ± 0.001 g on the intended axis, and 0.0019 ± 0.0006 g on the orthogonal axis, indicating only small deviation from linearity. To record spike tuning in neurons without spontaneous firing, a rheobase current was injected to depolarize the cell (<=40 pA, 12/15; >40 pA, 3/15).

Circular stimulation: clockwise (CW) and anticlockwise (CCW) 2 Hz circular movements with direction-varying acceleration of 0.02 g, were applied at the end of the recording to measure the dynamic neural response. CW and CCW stimuli have 90° phase difference in acceleration between X and Y axes.

Otolith afferent stimulation and pharmacology—A glass pipette electrode (2–5 MΩ) filled with extracellular solution ([in mM] NaCl 134, KCl 2.9, $MgCl_2$ 1.2, HEPES 10, glucose 10, $CaCl_2$ 2.1, osmolarity ~295 mOsm and pH ~7.5) was connected to a stimulator (A-M systems, Model 2100), and placed in the vestibular ganglion to stimulate the vestibular afferents. A train of 0.1 ms, 1 μA - 1 mA electrical pulses at varying frequencies were delivered to elicit EPSCs in the recorded cells. At least 20 trials of evoked EPSCs were recorded to establish a stable baseline. AMPA receptors and gap junctions were blocked with 10 μM NBQX and 500 μM carbenoxolone, respectively.

Electron Microscopy: Ultrathin serial sections of brainstem from a 5.5 dpf zebrafish were a generous loan from J. Lichtman and F. Engert. Using the published 18.8 × 18.8 × 60 nm^3 per voxel and 56.4 × 56.4 × 60 nm^3 per voxel reference map and reconstructions (Hildebrand et al., 2017), we targeted re-imaging at 4.0 × 4.0 × 60 nm^3 per voxel to the entirety of the myelinated utricular afferents (identified by their peripheral processes reaching for the utricular macula) and VS neurons (identified by their position and axonal projections into the spinal cord) on one side of the brainstem, covering ~95 μm in the rostrocaudal axis. Imaging was carried out on a Zeiss Merlin 540 FE-SEM with a solid-state backscatter detector. The ATLAS scan engine was controlled via WaferMapper (Hayworth et al., 2014). The resulting images were aligned onto the existing 56.4 × 56.4 × 60 nm^3 per voxel dataset using linear affine transformations in FIJI with the TrakEM2 plug-in (Cardona et al., 2012). In a small subset of identified synapses, we carried out further re-imaging at 1.0 × 1.0 × 60 nm^3 per voxel to visualize the hallmarks of gap junctions.

The existing reconstructions of myelinated portions of VS neurons and utricular afferents were extended to cover branches that had been missed in the original dataset. Appositions between afferents and VS neurons were considered to be synaptic contacts if the presynapse contained vesicles, the membranes were tightly apposed and straight, and there were signs of a postsynaptic density. In cases where appositions were more difficult to determine, such as those parallel to the plane of section, vesicle clustering at a tight apposition was used as the criterion for a synapse.

EPSP Modeling—Computational modeling was carried out in NEURON 7.6 (Hines and Carnevale, 1997). Because the goal was to test whether excitatory synaptic inputs were sufficient to explain the observed subthreshold tuning, only passive conductances were implemented. For each recorded neuron, input resistance measured by small hyperpolarizing steps was scaled by a fixed factor to define gLeak_hh, which was the only parameter adjusted in the model. EPSCs recorded during sensory stimulation were fed back into the model via a GClamp (dynamic clamp) mechanism (Bagnall et al., 2011) with a reversal potential of +40 mV. The resulting modeled EPSPs were then analyzed for direction and phase dynamics and compared to the same analysis on actual recorded EPSPs from the same neuron. The same approach was applied for spiking data with the addition of SpikeOut to evoke spikes at a given threshold (Brette, 2007), which was held consistent within neurons but adjusted from one neuron to the next to match the total number of spikes elicited during stimulation.

Quantification and statistical analysis:

All analysis was implemented with custom written codes in Matlab (Mathworks).

Event detection: EPSC events were detected by a derivative method (Bagnall and McLean, 2014). The electrical and chemical EPSCs were further separated using a deconvolution method (details described below). The kinetics of the fast EPSCs measured here were extremely rapid, with rise times around 0.4 ms and fall times similarly brief, consistent with their identity as largely electrical synaptic events (Fig. 2). As a consequence, we could reliably identify events with > 0.2 ms separation due to the change in rate of rise. The threshold for event identification was 6 pA.

Tuning index of all EPSCs was calculated as the vectoral sum of all events' phase, weighted by the EPSC amplitude.

$$Tuning\ index = \frac{\left|\sum A_j * e^{i * \theta_j}\right|}{\sum A_j}, i = \sqrt{-1}$$

(A_j is the amplitude of each EPSC event j, and θ_j is the phase of that event relative to the sinusoidal stimulus on each axis.)

Deconvolution analysis—Deconvolving EPSC signals not only separated EPSCs with different temporal kinetics, but also resolved overlapping events and gave more accurate amplitude measurements, because a kernel was used. We assumed that the signals we observed on voltage clamp were primarily composed of electrical EPSCs and chemical EPSCs from afferents, based on our observation from the pharmacology data.

$$S = conv(w_e, s_e) + conv(w_c, s_c) + residuals$$

(w_e, w_c) are the kernels of electrical and chemical components of EPSCs, both derived from their waveforms shown in Fig. 2, and s_e, s_c are the separated electrical and chemical signals)

A sparse deconvolution algorithm with L1 regularization, derived from FISTA (Beck and Teboulle, 2009), was applied to obtain s_e, s_c by minimizing the objective function:

$$F(s_e, s_c) \equiv \frac{1}{2}(S_{observed} - S_{reconstruct})^2 + \lambda_e * |s_e| + \lambda_c * |s_c|,$$

where:

$$S_{reconstruct} = conv(w_e, s_e) + conv(w_c, s_c)$$

λ_e and λ_c were defined by the root mean square of the signal and magnitude of kernel waveform: $\lambda_i = rms(S_{observed}) * \sqrt[2]{w_i * w_i^T}$. Maximum iteration cycle was set at 500

Clustering of electrical events—Amplitude-invariant EPSCs are mediated by gap junctions, therefore only electrical signals s_e were used to infer individual afferent inputs. A threshold of 3.5 * $std(s_e)$ was used for event detection. Detected electrical events were clustered by ISO-SPLIT (Chung et al., 2017). Some clusters were merged or split manually after examination. Clusters with refractory period (threshold: probability < 0.003 within 1 ms) in auto-correlograms (100 ms) were considered from an individual afferent.

For each cluster, the tuning vector of inferred afferent k on each linear axis was quantified as:

$$z_k = \frac{\sum e^{i * \theta_j}}{N_c * A_s} * f_s, i = \sqrt{-1}$$

(θ_j is the phase of EPSC event j in cluster k. N_c is the number of cycles for sinusoidal translation, f_s [Hz] and A_s [g] are the frequency and amplitude of the stimulus. The absolute value and argument of z represent the tuning gain and the tuning phase, respectively.)

Afferent input similarity index for a VS neuron was determined as:

$$\frac{|\sum A_k * z_k|}{\sum A_k * n_k}$$

(A_k, z_k, n_k are the average EPSC amplitude, tuning vector and number of events for cluster k.)

Tuning vector quantification—Tuning in four linear axes was fitted into a 2-dimensional spatiotemporal model (Angelaki, 1992) to obtain the maximum tuning direction A_{max} and the tuning gain S_{max}, phase P_{max} in that direction. In this model, the 2-dimensional tuning of an individual afferent is described by two vectors T_{max} and T_{min} that are spatially and temporally orthogonal to each other ($A_{max} = A_{min} \pm 90°$, $P_{max} = P_{min} \pm 90°$) When the tuning is measured on a particular axis at A degrees, the tuning gain S for fitting is determined by

$$S_f^2 = S_{max}^2 * \cos^2(A_{max} - A) + S_{min}^2 * \sin^2(A_{max} - A)$$

The tuning phase P for fitting is determined by the argument of $z = a + b * i(i = \sqrt{-1})$, where:

$$a = S_{max} * \cos(A - A_{max}) * \cos(P_{max}) + S_{min} * \sin(A - A_{max}) * \cos(P_{min})$$

$$b = S_{max} * \cos(A - A_{max}) * \sin(P_{max}) + S_{min} * \sin(A - A_{max}) * \sin(P_{min})$$

The gain and phase of T_{max} and T_{min} are fitted by:

$$\min \sum_{j = 1}^{4} \left(S_j - S_f\left(A_j\right)\right)^2$$

$$\min \sum_{j = 1}^{4} \left(z_j - z\left(A_j\right)\right)^2, z_j = \left|z\left(A_j\right)\right| * e^{i\left(P_j\right)}$$

AC/DC response quantification—AC of membrane potential and spiking response were defined as the amplitude of sinusoidal fit (2 Hz) of the membrane potential, and the spike vectorial sum during sensory stimulation, respectively. DC of membrane potential and spiking response were defined as the average membrane potential during sensory stimulation above baseline (no stimulation), and the total spike number during sensory stimulation above baseline. For spiking responses, VS neurons with firing rate > 4 spike/cycle and spike AC or DC >1 spike/cycle were included in the analysis.

Bootstrapping: $\binom{n_i}{2}$ afferent pairs were counted for VS neuron i with n_i distinct afferent inputs ($n_i \geq 2$). The same number of total afferent pairs $\sum_{i = 1}^{m} \binom{n_i}{2}$ from all m VS neurons was randomly selected among all $\sum_{i = 1}^{m} n_i$ inferred afferents to determine the convergence angle or phase difference distribution by chance, and such selection was performed 5000 times to calculate mean and standard deviation.

Statistics—Statistical methods used for testing, number of data, and p values are reported in the corresponding figure legends. Groups numbers were reported as mean ± STD, unless stated otherwise.

Supplementary Material

Refer to Web version on PubMed Central for supplementary material.

Acknowledgments

We are grateful to Dr. Timothy Holy for guidance on development of EPSC analysis and valuable feedback on the project. We thank Dr. Richard Roberts for helping set up the electrophysiology recording rig, and Drs. Rebecca Callahan, Mohini Sengupta and Mr. Saul Bello Rojas for thoughtful critiques of the paper. Drs. Daniel Kerschensteiner and David Schoppik also contributed insightful comments on the manuscript. We also acknowledge the Washington University Zebrafish Facility for fish care and Washington University Center for Cellular Imaging

(WUCCI) for supporting the confocal imaging experiments. This work is supported by funding through the National Institute of Health (NIH) R00 DC012536 (M.W.B.), R01 DC016413 (M.W.B.), R21EY030623 (J.L.M.), a Sloan Research Fellowship (M.W.B.), a Leon Levy Foundation Fellowship in Neuroscience (D.G.C.H.), and the National BioResource Project in Japan (S.H.). M.W.B. is a Pew Biomedical Scholar and a McKnight Foundation Scholar. J.L.M is a recipient of a Research to Prevent Blindness Career Development Award.

References:

AKROUH A & KERSCHENSTEINER D 2013 Intersecting Circuits Generate Precisely Patterned Retinal Waves. Neuron, 79, 322–334. [PubMed: 23830830]

ALONSO JM & MARTINEZ LM 1998 Functional connectivity between simple cells and complex cells in cat striate cortex. Nature Neuroscience, 1, 395–403. [PubMed: 10196530]

ANGELAKI DE 1992 SPATIOTEMPORAL CONVERGENCE (STC) IN OTOLITH NEURONS. Biological Cybernetics, 67, 83–96. [PubMed: 1606247]

ANGELAKI DE, BUSH GA & PERACHIO AA 1993 2-DIMENSIONAL SPATIOTEMPORAL CODING OF LINEAR ACCELERATION IN VESTIBULAR NUCLEI NEURONS. Journal of Neuroscience, 13, 1403–1417. [PubMed: 8463828]

ANGELAKI DE & CULLEN KE 2008 Vestibular system: The many facets of a multimodal sense. Annual Review of Neuroscience, 31, 125–150.

ANGELAKI DE & DICKMAN JD 2000 Spatiotemporal processing of linear acceleration: Primary afferent and central vestibular neuron responses. Journal of Neurophysiology, 84, 2113–2132. [PubMed: 11024100]

ARENZ A, SILVER RA, SCHAEFER AT & MARGRIE TW 2008 The contribution of single synapses to sensory representation in vivo. Science, 321, 977–80. [PubMed: 18703744]

BAGNALL MW, HULL C, BUSHONG EA, ELLISMAN MH & SCANZIANI M 2011 Multiple Clusters of Release Sites Formed by Individual Thalamic Afferents onto Cortical Interneurons Ensure Reliable Transmission. Neuron, 71, 180–194. [PubMed: 21745647]

BAGNALL MW, MCELVAIN LE, FAULSTICH M & DU LAC S 2008 Frequency-independent synaptic transmission supports a linear vestibular behavior. Neuron, 60, 343–52. [PubMed: 18957225]

BAGNALL MW & MCLEAN DL 2014 Modular organization of axial microcircuits in zebrafish. Science (New York, N.Y.), 343, 197–200.

BAGNALL MW & SCHOPPIK D 2018 Development of vestibular behaviors in zebrafish. Current Opinion in Neurobiology, 53, 83–89. [PubMed: 29957408]

BECK A & TEBOULLE M 2009 A Fast Iterative Shrinkage-Thresholding Algorithm for Linear Inverse Problems. Siam Journal on Imaging Sciences, 2, 183–202.

BIANCO IH, MA LH, SCHOPPIK D, ROBSON DN, ORGER MB, BECK JC, LI JM, SCHIER AF, ENGERT F & BAKER R 2012 The tangential nucleus controls a gravito-inertial vestibulo-ocular reflex. Current Biology, 22, 1285–1295. [PubMed: 22704987]

BOYLE R, GOLDBERG JM & HIGHSTEIN SM 1992 Inputs from regularly and irregularly discharging vestibular nerve afferents to secondary neurons in squirrel monkey vestibular nuclei. III. Correlation with vestibulospinal and vestibuloocular output pathways. J Neurophysiol, 68, 471–84. [PubMed: 1527570]

BOYLE R & JOHANSON C 2003 Morphological properties of vestibulospinal neurons in primates. Annals of the New York Academy of Sciences, 1004, 183–195. [PubMed: 14662458]

BRETTE R 2007 Exact simulation of integrate-and-fire models with exponential currents. Neural Computation, 19, 2604–2609. [PubMed: 17716004]

BRUNO RM, KHATRI V, LAND PW & SIMONS DJ 2003 Thalamocortical angular tuning domains within individual barrels of rat somatosensory cortex. Journal of Neuroscience, 23, 9565–9574. [PubMed: 14573536]

BUDELLI R & MACADAR O 1979 STATO-ACOUSTIC PROPERTIES OF UTRICULAR AFFERENTS. Journal of Neurophysiology, 42, 1479–1493. [PubMed: 490203]

CARDONA A, SAALFELD S, SCHINDELIN J, ARGANDA-CARRERAS I, PREIBISCH S, LONGAIR M, TOMANCAK P, HARTENSTEIN V & DOUGLAS RJ 2012 TrakEM2 Software for Neural Circuit Reconstruction. Plos One, 7.

CHABROL FP, ARENZ A, WIECHERT MT, MARGRIE TW & DIGREGORIO DA 2015 Synaptic diversity enables temporal coding of coincident multisensory inputs in single neurons. Nat Neurosci, 18, 718–27. [PubMed: 25821914]

CHUNG JE, MAGLAND JF, BARNETT AH, TOLOSA VM, TOOKER AC, LEE KY, SHAH KG, FELIX SH, FRANK LM & GREENGARD LF 2017 A Fully Automated Approach to Spike Sorting. Neuron, 95, 1381–1394 e6. [PubMed: 28910621]

CULLEN KE 2019 Vestibular processing during natural self-motion: implications for perception and action. Nature Reviews Neuroscience, 20, 346–363. [PubMed: 30914780]

EATOCK RA & SONGER JE 2011 Vestibular hair cells and afferents: two channels for head motion signals. Annu Rev Neurosci, 34, 501–34. [PubMed: 21469959]

EHRLICH DE & SCHOPPIK D 2017 Control of Movement Initiation Underlies the Development of Balance. Current Biology, 27, 334–344. [PubMed: 28111151]

EHRLICH DE & SCHOPPIK D 2019 A primal role for the vestibular sense in the development of coordinated locomotion. Elife, 8.

FAVRE-BULLE IA, VANWALLEGHEM G, TAYLOR MA, RUBINSZTEIN-DUNLOP H & SCOTT EK 2018 Cellular-Resolution Imaging of Vestibular Processing across the Larval Zebrafish Brain. Curr Biol, 28, 3711–3722 e3. [PubMed: 30449665]

FAY RR 1984 THE GOLDFISH EAR CODES THE AXIS OF ACOUSTIC PARTICLE MOTION IN 3 DIMENSIONS. Science, 225, 951–954. [PubMed: 6474161]

FELLEMAN DJ & VAN ESSEN DC 1991 Distributed Hierarchical Processing in the Primate Cerebral Cortex. Cerebral Cortex, 1, 1–47. [PubMed: 1822724]

FERNANDEZ C & GOLDBERG JM 1976a PHYSIOLOGY OF PERIPHERAL NEURONS INNERVATING OTOLITH ORGANS OF SQUIRREL-MONKEY. 1. RESPONSE TO STATIC TILTS AND TO LONG-DURATION CENTRIFUGAL FORCE. Journal of Neurophysiology, 39, 970–984. [PubMed: 824412]

FERNANDEZ C & GOLDBERG JM 1976b PHYSIOLOGY OF PERIPHERAL NEURONS INNERVATING OTOLITH ORGANS OF SQUIRREL-MONKEY. 3. RESPONSE DYNAMICS. Journal of Neurophysiology, 39, 996–1008. [PubMed: 824414]

FERNANDEZ C, GOLDBERG JM & ABEND WK 1972 RESPONSE TO STATIC TILTS OF PERIPHERAL NEURONS INNERVATING OTOLITH ORGANS OF SQUIRREL-MONKEY. Journal of Neurophysiology, 35, 978–+. [PubMed: 4631840]

GOLDBERG JM, DESMADRYL G, BAIRD RA & FERNANDEZ C 1990 THE VESTIBULAR NERVE OF THE CHINCHILLA. 4. DISCHARGE PROPERTIES OF UTRICULAR AFFERENTS. Journal of Neurophysiology, 63, 781–790. [PubMed: 2341876]

HADDON C, MOWBRAY C, WHITFIELD T, JONES D, GSCHMEISSNER S & LEWIS J 1999 Hair cells without supporting cells: further studies in the ear of the zebrafish mind bomb mutant. J Neurocytol, 28, 837–50. [PubMed: 10900088]

HAYWORTH KJ, MORGAN JL, SCHALEK R, BERGER DR, HILDEBRAND DGC & LICHTMAN JW 2014 Imaging ATUM ultrathin section libraries with WaferMapper: a multi-scale approach to EM reconstruction of neural circuits. Frontiers in Neural Circuits, 8.

HILDEBRAND DGC, CICCONET M, TORRES RM, CHOI W, QUAN TM, MOON J, WETZEL AW, SCOTT CHAMPION A, GRAHAM BJ, RANDLETT O, PLUMMER GS, PORTUGUES R, BIANCO IH, SAALFELD S, BADEN AD, LILLANEY K, BURNS R, VOGELSTEIN JT, SCHIER AF, LEE WA, JEONG WK, LICHTMAN JW & ENGERT F 2017 Whole-brain serial-section electron microscopy in larval zebrafish. Nature, 545, 345–349. [PubMed: 28489821]

HINES ML & CARNEVALE NT 1997 The NEURON simulation environment. Neural Computation, 9, 1179–1209. [PubMed: 9248061]

HUBEL DH & WIESEL TN 1962 RECEPTIVE FIELDS, BINOCULAR INTERACTION AND FUNCTIONAL ARCHITECTURE IN CATS VISUAL CORTEX. Journal of Physiology-London, 160, 106–&.

JAMALI M, CARRIOT J, CHACRON MJ & CULLEN KE 2013 Strong Correlations between Sensitivity and Variability Give Rise to Constant Discrimination Thresholds across the Otolith Afferent Population. Journal of Neuroscience, 33, 11302–11313. [PubMed: 23825433]

JIA H, ROCHEFORT NL, CHEN X & KONNERTH A 2010 Dendritic organization of sensory input to cortical neurons in vivo. Nature, 464, 1307–1312. [PubMed: 20428163]

KIMMEL CB, POWELL SL & METCALFE WK 1982 Brain neurons which project to the spinal cord in young larvae of the zebrafish. The Journal of comparative neurology, 205, 112–27. [PubMed: 7076887]

KIMURA Y, HISANO Y, KAWAHARA A & HIGASHIJIMA S 2014 Efficient generation of knock-in transgenic zebrafish carrying reporter/driver genes by CRISPR/Cas9-mediated genome engineering. Scientific Reports, 4.

KODAMA T, GITTIS A, SHIN M, KELLEHER K, KOLKMAN K, MCELVAIN L, LAM M & DU LAC S 2020 Graded co-expression of ion channel, neurofilament, and synaptic genes in fast-spiking vestibular nucleus neurons. J Neurosci.

KORN H, SOTELO C & BENNETT MVL 1977 The lateral vestibular nucleus of the toadfish Opsanus tau: Ultrastructural and electrophysiological observations with special reference to electrotonic transmission. Neuroscience.

LAURENS J, LIU S, YU XJ, CHAN R, DICKMAN D, DEANGELIS GC & ANGELAKI DE 2017 Transformation of spatiotemporal dynamics in the macaque vestibular system from otolith afferents to cortex. Elife, 6.

LAVZIN M, RAPOPORT S, POLSKY A, GARION L & SCHILLER J 2012 Nonlinear dendritic processing determines angular tuning of barrel cortex neurons in vivo. Nature, 490, 397–401. [PubMed: 22940864]

LECUN Y, BENGIO Y & HINTON G 2015 Deep learning. Nature, 521, 436–444. [PubMed: 26017442]

LU Z, XU Z & BUCHSER WJ 2004 Coding of acoustic particle motion by utricular fibers in the sleeper goby, Dormitator latifrons. Journal of Comparative Physiology a-Neuroethology Sensory Neural and Behavioral Physiology, 190, 923–938.

LUNSFORD ET, SKANDALIS DA & LIAO JC 2019 Efferent modulation of spontaneous lateral line activity during and after zebrafish motor commands. Journal of Neurophysiology, 122, 2438–2448. [PubMed: 31642405]

MARUSKA KP & MENSINGER AF 2015 Directional sound sensitivity in utricular afferents in the toadfish Opsanus tau. Journal of Experimental Biology, 218, 1759–1766. [PubMed: 25883378]

MCELVAIN LE, FAULSTICH M, JEANNE JM, MOORE JD & DU LAC S 2015 Implementation of linear sensory signaling via multiple coordinated mechanisms at central vestibular nerve synapses. Neuron, 85, 1132–44. [PubMed: 25704949]

MCLEAN DL & FETCHO JR 2009 Spinal Interneurons Differentiate Sequentially from Those Driving the Fastest Swimming Movements in Larval Zebrafish to Those Driving the Slowest Ones. Journal of Neuroscience, 29, 13566–13577. [PubMed: 19864569]

MIGAULT G, VAN DER PLAS TL, TRENTESAUX H, PANIER T, CANDELIER R, PROVILLE R, ENGLITZ B, DEBREGEAS G & BORMUTH V 2018 Whole-Brain Calcium Imaging during Physiological Vestibular Stimulation in Larval Zebrafish. Curr Biol, 28, 3723–3735 e6. [PubMed: 30449666]

MO W, CHEN FY, NECHIPORUK A & NICOLSON T 2010 Quantification of vestibular-induced eye movements in zebrafish larvae. Bmc Neuroscience, 11.

NAGY JI, BAUTISTA W, BLAKLEY B & RASH JE 2013 Morphologically mixed chemical-electrical synapses formed by primary afferents in rodent vestibular nuclei as revealed by immunofluorescence detection of connexin36 and vesicular glutamate transporter-1. Neuroscience, 252, 468–88. [PubMed: 23912039]

NEUHUBER WL & ZENKER W 1989 CENTRAL DISTRIBUTION OF CERVICAL PRIMARY AFFERENTS IN THE RAT, WITH EMPHASIS ON PROPRIOCEPTIVE PROJECTIONS TO VESTIBULAR, PERIHYPOGLOSSAL, AND UPPER THORACIC SPINAL NUCLEI. Journal of Comparative Neurology, 280, 231–253. [PubMed: 2466876]

NEWLANDS SD & PERACHIO AA 2003 Central projections of the vestibular nerve: a review and single fiber study in the Mongolian gerbil. Brain Research Bulletin, 60, 475–495. [PubMed: 12787868]

ORLOVSKY GN 1972 ACTIVITY OF VESTIBULOSPINAL NEURONS DURING LOCOMOTION. Brain Research, 46, 85–&. [PubMed: 4635375]

PEREDA AE 2016 Developmental functions of electrical synapses. Journal of Physiology-London, 594, 2561–2562.

PETERSEN CCH 2007 The functional organization of the barrel cortex. Neuron, 56, 339–355. [PubMed: 17964250]

PETERSON BW 1970 Distribution of neural responses to tilting within vestibular nuclei of the cat. J Neurophysiol, 33, 750–67. [PubMed: 5485402]

PICHLER P & LAGNADO L 2020 Motor Behavior Selectively Inhibits Hair Cells Activated by Forward Motion in the Lateral Line of Zebrafish. Current Biology, 30, 150–+. [PubMed: 31866371]

PLATT C 1977 HAIR CELL DISTRIBUTION AND ORIENTATION IN GOLDFISH OTOLITH ORGANS. Journal of Comparative Neurology, 172, 283–297. [PubMed: 838883]

PRIEBE NJ & FERSTER D 2012 Mechanisms of Neuronal Computation in Mammalian Visual Cortex. Neuron, 75, 194–208. [PubMed: 22841306]

PRIEBE NJ, MECHLER F, CARANDINI M & FERSTER D 2004 The contribution of spike threshold to the dichotomy of cortical simple and complex cells. Nature Neuroscience, 7, 1113–1122. [PubMed: 15338009]

RILEY BB & MOORMAN SJ 2000 Development of utricular otoliths, but not saccular otoliths, is necessary for vestibular function and survival in zebrafish. J Neurobiol, 43, 329–37. [PubMed: 10861559]

ROBERTS R, ELSNER J & BAGNALL MW 2017 Delayed Otolith Development Does Not Impair Vestibular Circuit Formation in Zebrafish. J Assoc Res Otolaryngol, 18, 415–425. [PubMed: 28332011]

ROY NC, BESSAIH T & CONTRERAS D 2011 Comprehensive mapping of whisker-evoked responses reveals broad, sharply tuned thalamocortical input to layer 4 of barrel cortex. Journal of Neurophysiology, 105, 2421–2437. [PubMed: 21325677]

SARKISIAN VH 2000 Input-output relations of Deiters' lateral vestibulospinal neurons with different structures of the brain. Archives Italiennes De Biologie, 138, 295–353. [PubMed: 11116571]

SCHOPPIK D, BIANCO IH, PROBER DA, DOUGLASS AD, ROBSON DN, LI JMB, GREENWOOD JSF, SOUCY E, ENGERT F & SCHIER AF 2017 Gaze-Stabilizing Central Vestibular Neurons Project Asymmetrically to Extraocular Motoneuron Pools. J Neurosci, 37, 11353–11365. [PubMed: 28972121]

SCHOR RH, MILLER AD & TOMKO DL 1984 Responses to head tilt in cat central vestibular neurons. I. Direction of maximum sensitivity. J Neurophysiol, 51, 136–46. [PubMed: 6319622]

SHERMAN SM 2005 Thalamic relays and cortical functioning In: CASAGRANDE VA, GUILLERY RW & SHERMAN SM (eds.) Cortical Function: a View from the Thalamus.

SKOTTUN BC, DE VALOIS RL, GROSOF DH, MOVSHON JA, ALBRECHT DG & BONDS AB 1991 Classifying simple and complex cells on the basis of response modulation. Vision Res, 31, 1079–86. [PubMed: 1909826]

SMEAR MC, TAO HZW, STAUB W, ORGER MB, GOSSE NJ, LIU Y, TAKAHASHI K, POO MM & BAIER H 2007 Vesicular glutamate transport at a central synapse limits the acuity of visual perception in zebrafish. Neuron, 53, 65–77. [PubMed: 17196531]

STRAKA H & DIERINGER N 1996 Uncrossed disynaptic inhibition of second-order vestibular neurons and its interaction with monosynaptic excitation from vestibular nerve afferent fibers in the frog. Journal of Neurophysiology, 76, 3087–3101. [PubMed: 8930257]

TOMKO DL, PETERKA RJ & SCHOR RH 1981 RESPONSES TO HEAD TILT IN CAT 8TH NERVE AFFERENTS. Experimental Brain Research, 41, 216–221. [PubMed: 7215485]

TURECEK J, JACKMAN SL & REGEHR WG 2017 Synaptotagmin 7 confers frequency invariance onto specialized depressing synapses. Nature, 551, 503–506. [PubMed: 29088700]

USREY WM, REPPAS JB & REID RC 1999 Specificity and strength of retinogeniculate connections. Journal of Neurophysiology, 82, 3527–3540. [PubMed: 10601479]

VOESENEK CJ, PIETERS RPM & VAN LEEUWEN JL 2016 Automated Reconstruction of Three-Dimensional Fish Motion, Forces, and Torques. Plos One, 11.

WANG WC & MCLEAN DL 2014 Selective Responses to Tonic Descending Commands by Temporal Summation in a Spinal Motor Pool. Neuron, 83, 708–721. [PubMed: 25066087]

WILENT WB & CONTRERAS D 2005 Dynamics of excitation and inhibition underlying stimulus selectivity in rat somatosensory cortex. Nature Neuroscience, 8, 1364–1370. [PubMed: 16158064]

WITTS EC & MURRAY AJ 2019 Vestibulospinal contributions to mammalian locomotion. Current Opinion in Physiology, 8.

Highlights

- Recorded tuning of both vestibular inputs and their central targets in zebrafish
- Similarly tuned inputs tended to converge together
- Less frequently, inputs with different tuning converged postsynaptically
- Postsynaptic tuning could largely be explained as a summation of excitatory inputs

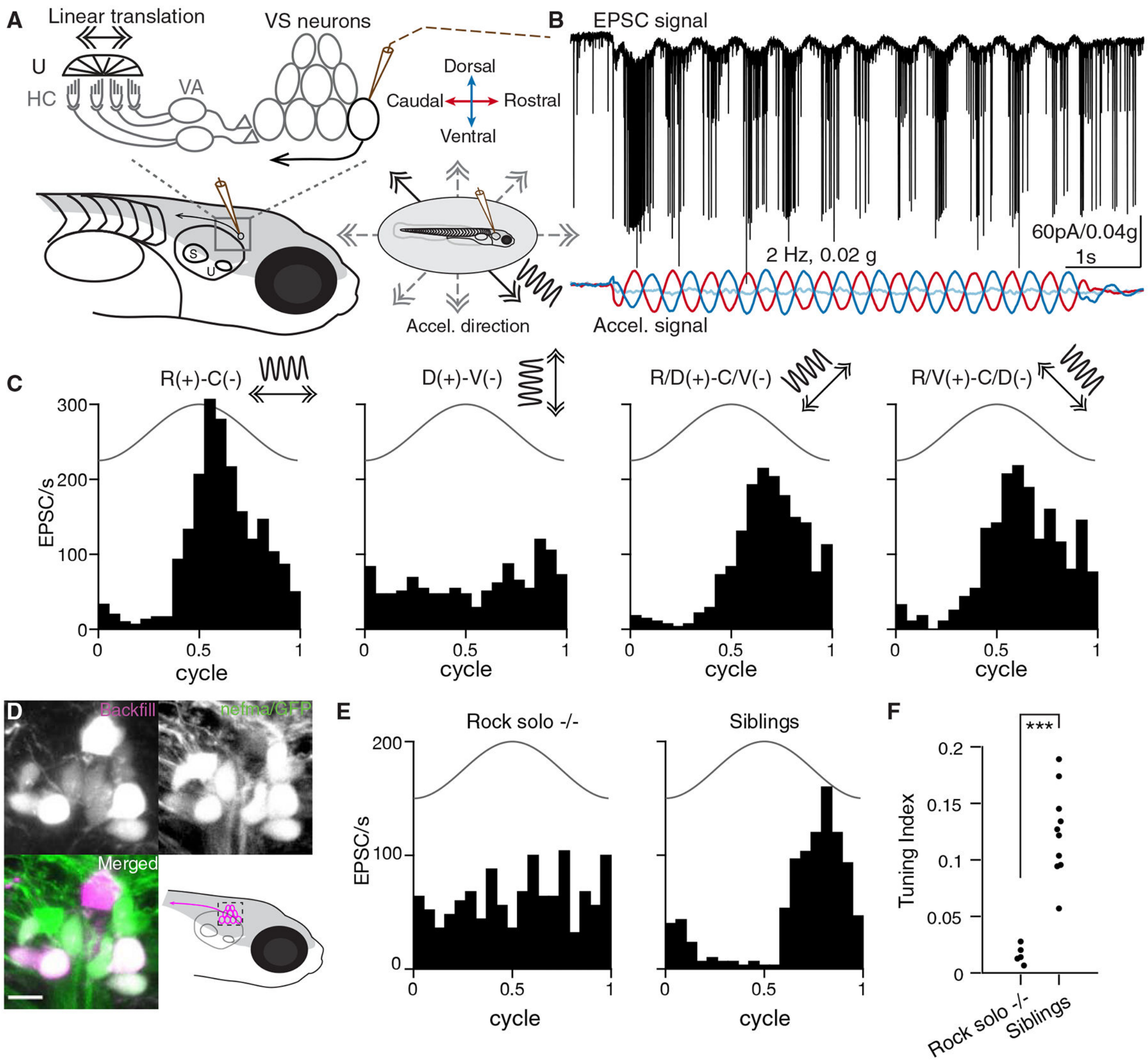

Figure 1:

Sensory-evoked responses *in vivo* in vestibulospinal (VS) neurons

A. Schematic representing *in vivo* patch clamp recording configuration and vestibular afferent circuit in larval zebrafish, U: utricle, HC: hair cells, VA: vestibular afferents, S: saccule. Inset, vestibular stimuli were delivered by a motorized table, acceleration direction indicated by the arrows and waveform by the sinusoidal curve. Solid, stimulus direction same as in B; dashed, other stimulus directions.

B. Example recording trace from a VS neuron in voltage clamp (V_{hold}: −65 mV) during 2 Hz, 0.02 g translational movement on the R/V(+)-C/D(−) axis. Membrane current and EPSC frequency are modulated by the translational movement. Black, EPSCs; colored, acceleration (same as in A) in three body axes recorded by an accelerometer (red, (R)ostral[+]-(C)audal[−]; dark blue, (D)orsal[+]-(V)entral[-]; light blue, (I)psilateral[+]-(C)ontralateral[−]).

C. Sensory-evoked EPSC responses to translation in four different directions for the same VS neuron as in B, across 12 cycles. Solid line, acceleration (2 Hz, 0.02 g).

D. Tg(nefma:gal4; UAS:GFP) (green) colabels VS neurons identified by dye backfilling (magenta) from spinal cord. Scale bar: 5 μm

E. Sensory responses of a VS neuron in the best direction in a rock solo −/− (left) and in a het/WT sibling (right).

F. Summary of tuning index in the best direction for all VS neurons recorded in rock solo −/− (9 neurons, 5 fish) and siblings (15 neurons, 10 fish). Mann-Whitney U test, p=6.7e-4

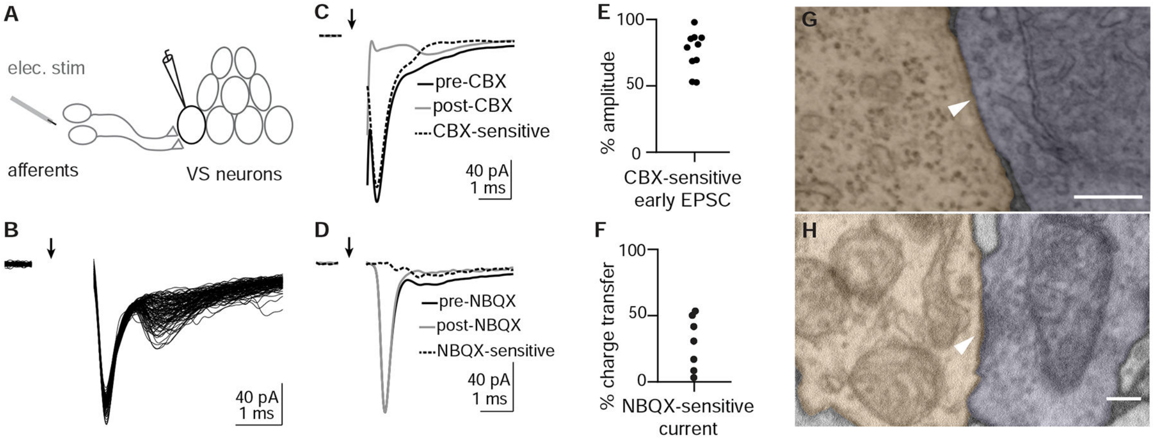

Figure 2:

Otolith afferent to VS neuron transmission is mediated by mixed electrical and chemical synapses

A. Schematic of whole-cell recording configuration from VS neuron while electrically stimulating otolith afferents.

B. Example EPSCs evoked by electrical stimulation of the otolith afferents; 105 EPSCs overlaid. Arrow indicates onset of stimulation. Stimulus artifact is blanked.

C. Carbenoxolone (CBX) diminishes the fast component of evoked EPSCs while slower component remains. Average traces from an example VS neuron; pre-CBX, n=100; post-CBX, n=100.

D. NBQX abolishes the second, slower component of evoked EPSCs without diminishing the early component. Pre-NBQX, n=349; post-NBQX, n=333.

E. Group data quantifying the reduction of early EPSC amplitude by CBX, n=10.

F. Group data quantifying the total charge transfer that is abolished by NBQX application, n=7.

G. Example EM image of gap junction between identified otolith afferent (pseudocolored purple) and VS neuron (peach), recognizable by the tight apposition of membranes to the exclusion of extracellular space,. Scale bar: 200 nm.

H. Example EM image of chemical synapse between otolith afferent (purple) and VS neuron (peach), characterized by the presence of synaptic vesicles, postsynaptic density, and parallel membranes at the cleft. Scale bar: 200 nm.

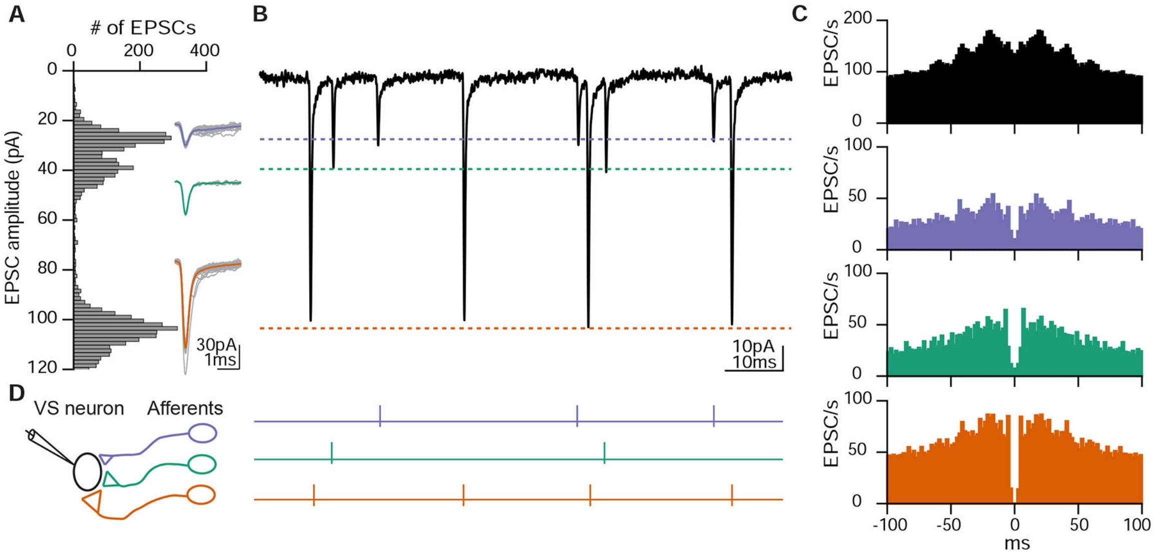

Figure 3:

Distinct EPSC amplitudes reflect individual afferent inputs

A. Histogram of spontaneous and sensory-evoked EPSC amplitude distribution of the same VS neuron as Fig. 1B. Inset, overlay of individual EPSCs (gray) and average (colored) for each amplitude bin.

B. Example trace of EPSCs exhibiting stereotypic shapes and amplitudes in three clusters, corresponding to each amplitude bin in A.

C. Auto-correlogram of all EPSCs recorded from the VS neuron (top, black) or divided into three clusters based on EPSC amplitudes (bottom, colored). Note EPSC activities around 0 ms only appears across all EPSCs, but not within each cluster.

D. Schematic of three different otolith afferents converging onto one VS neuron, each eliciting EPSCs with a distinct amplitude (represented by different synaptic sizes). Right, spike activities of three afferents inferred from B.

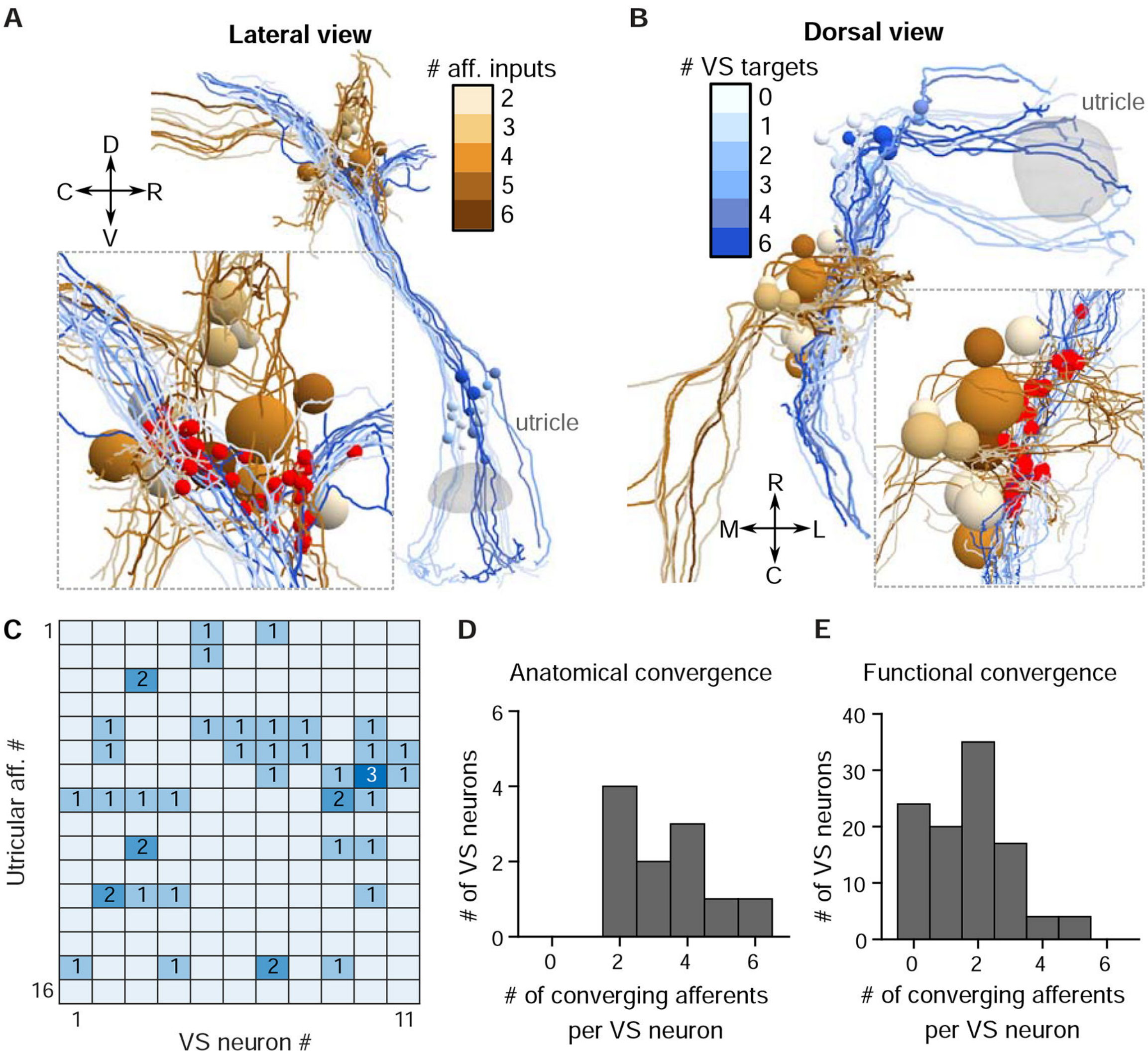

1					1		1				
					1						
			2								
		1			1	1	1	1		1	
		1				1	1	1		1	1
							1		1	3	1
	1	1	1	1					2	1	
			2						1	1	
		2	1	1						1	
	1			1			2		1		
16											
	1										11

Figure 4:

Anatomical reconstructions reveal a similar convergence pattern as physiology

A. Serial-section EM reconstruction (lateral view) of all myelinated utricular afferents (blues) and VS neurons (browns) on the right side of one animal (5.5 dpf). Inset, identified synaptic contacts between afferents and VS neurons (red). Color scale represents number of distinct afferents synapsing with a given VS neuron (browns). VS neurons with greater number of afferent inputs are located more ventrally.

B. Dorsal view of the same reconstruction as in A. Color scale represents number of VS neurons contacted by a given afferent (blues).

C. Number of distinct synaptic contacts from each utricular afferent onto each VS neuron, based on serial-section EM reconstruction.

D. Histogram of the numbers of distinct afferents converging onto each VS neuron, as measured by serial-section EM reconstruction (11 neurons, 1 fish)

E. Histogram of the numbers of distinct afferents converging onto each VS neuron, as inferred from whole-cell physiology recording (104 neurons, 89 fish)

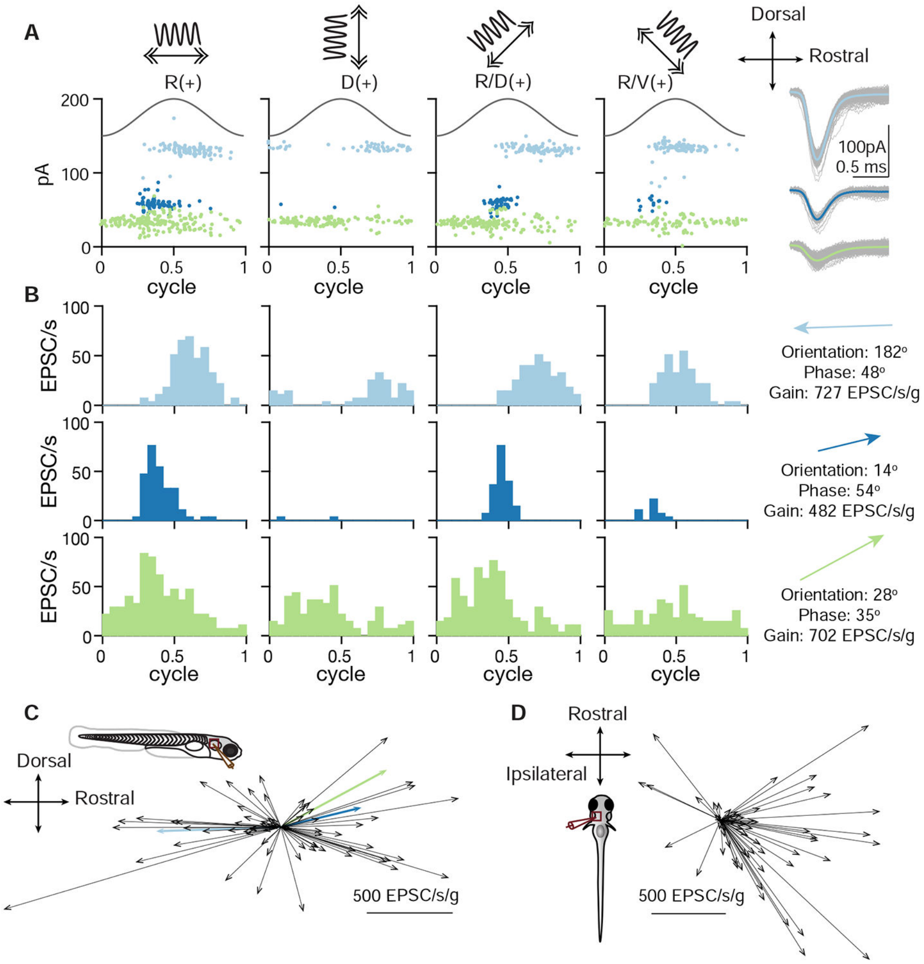

Figure 5:

Spatial tuning of inferred otolith afferents

A. EPSC responses of an example neuron in response to 2 Hz, 0.02 g translational stimuli (solid sinusoidal line, acceleration) along 4 different axes (top, arrows). Each dot represents one EPSC; note three EPSC clusters with distinct amplitudes. Right, overlay of individual EPSCs (gray) and average (colored) for each cluster.

B. EPSC tuning of three clusters. Right, vectors representing the maximum tuning direction, phase, and gain of each inferred afferent corresponding to an EPSC cluster.

C. Maximum tuning directions of all afferents from VS neurons recorded from fish oriented side-up. Colored arrows represent tuning of afferents in B (69 afferents, 43 neurons, 33 fish).

D. Maximum tuning directions of all inferred afferents from VS neurons recorded from fish oriented dorsal-up (60 afferents, 36 neurons, 36 fish).

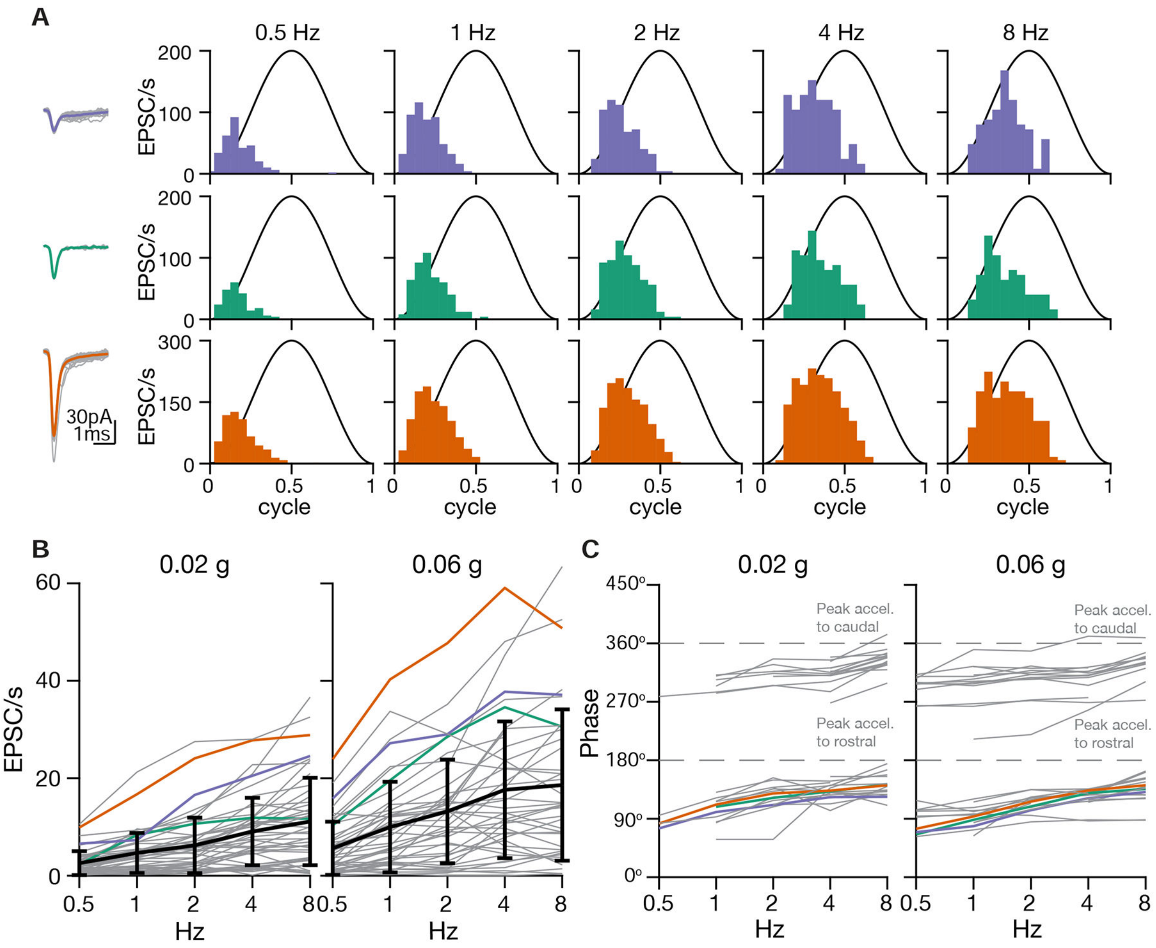

Figure 6:

Temporal tuning of inferred otolith afferents

A. Sensory tuning of afferent inputs to one VS neuron during translational movement at 5 different frequencies in the R(+)-C(−) axis. Left, EPSC waveforms of three different clusters recorded from one VS neuron. Right, temporal tuning profile of each EPSC cluster on the R-C axis.

B. Gains of inferred afferents across different frequencies of translational acceleration. Gray, individual afferents; colored, afferents from A; black, mean and standard deviation of gains from all afferents (0.02 g, 48 afferents; 0.06 g: 46 afferents; 25 neurons, 20 fish)

C. Phases of inferred afferents across frequencies, relative to the sinusoidal stimulus. 180° (0.5 cycle in A) represents the peak of acceleration towards rostral direction; 360° represents the peak of acceleration towards caudal direction (0 or 1 cycle in A). Data were thresholded to only include afferents whose gain was > 5 EPSC/s (0.02 g, 36 afferents; 0.06 g, 38 afferents; 25 neurons, 20 fish)

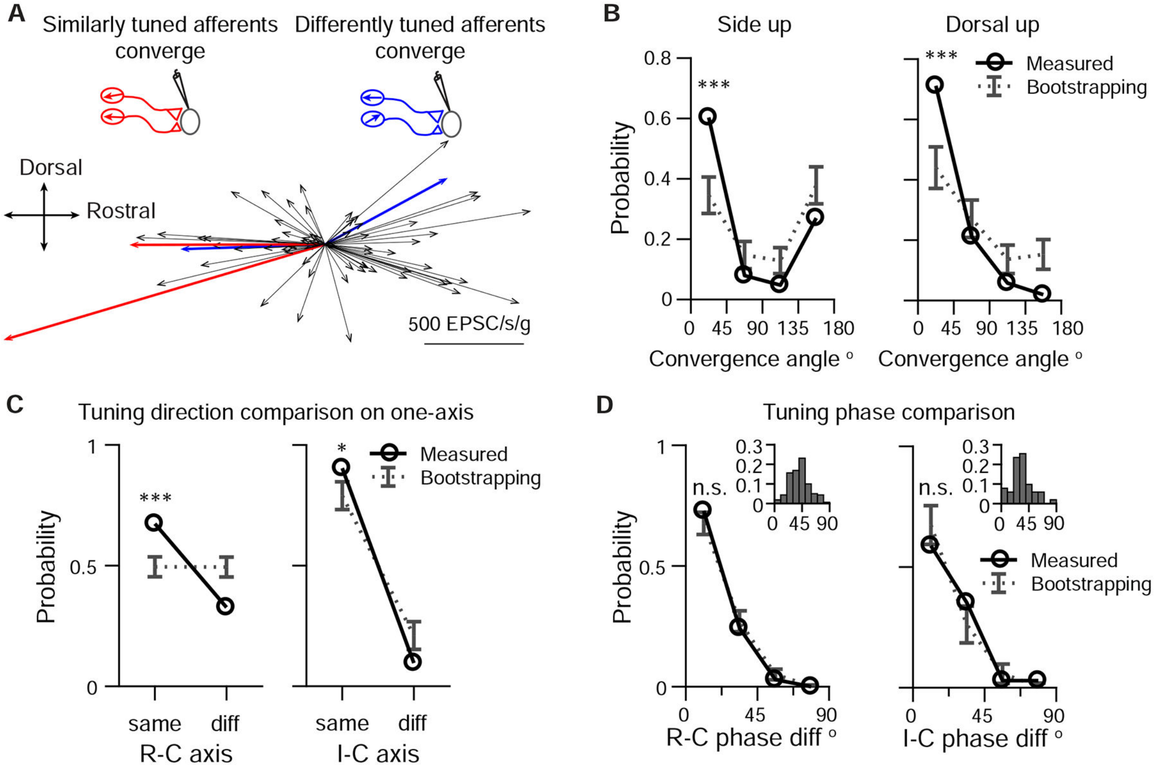

Figure 7:

Afferents with similar tuning direction preferentially converge

A. Example of two pairs of converging afferents from two VS neurons in side-up fish. Red, converging afferents are similarly tuned, with small converging angle between the pair; Blue: converging afferents are differently tuned, with large convergent angle between the pair.

B. Probability distribution of converging angles for measured and randomly generated afferents pairs in side-up fish and dorsal-up fish. Two tailed z-test, side up, 0–45°: p=2e-5, 135–180°: p=0.08. (63 afferent pairs); dorsal up, 0–45°: p=8e-5, 135–180°: p=0.007. (52 afferent pairs)

C. Probability distribution of converging afferents tuned to the same direction vs different direction, on the R-C and I-C axis. Two tailed z-test, R-C, same: p=1e-5, diff: p=4e-5 (150 afferent pairs); I-C, same: p=0.044, diff: p=0.044 (52 afferent pairs).

D. Probability distribution of phase difference for converging afferents, on the R-C and I-C axis. Two tailed z-test, R-C, 0–22.5° p=0.26 (103 afferent pairs); I-C, 0–22.5°, p=0.28 (34 afferent pairs). Inset: distribution of tuning phase of afferents, R-C, 177 afferents; I-C, 60 afferents; 90° represents the peak of acceleration of preferred direction (2 Hz, 0.02 g).

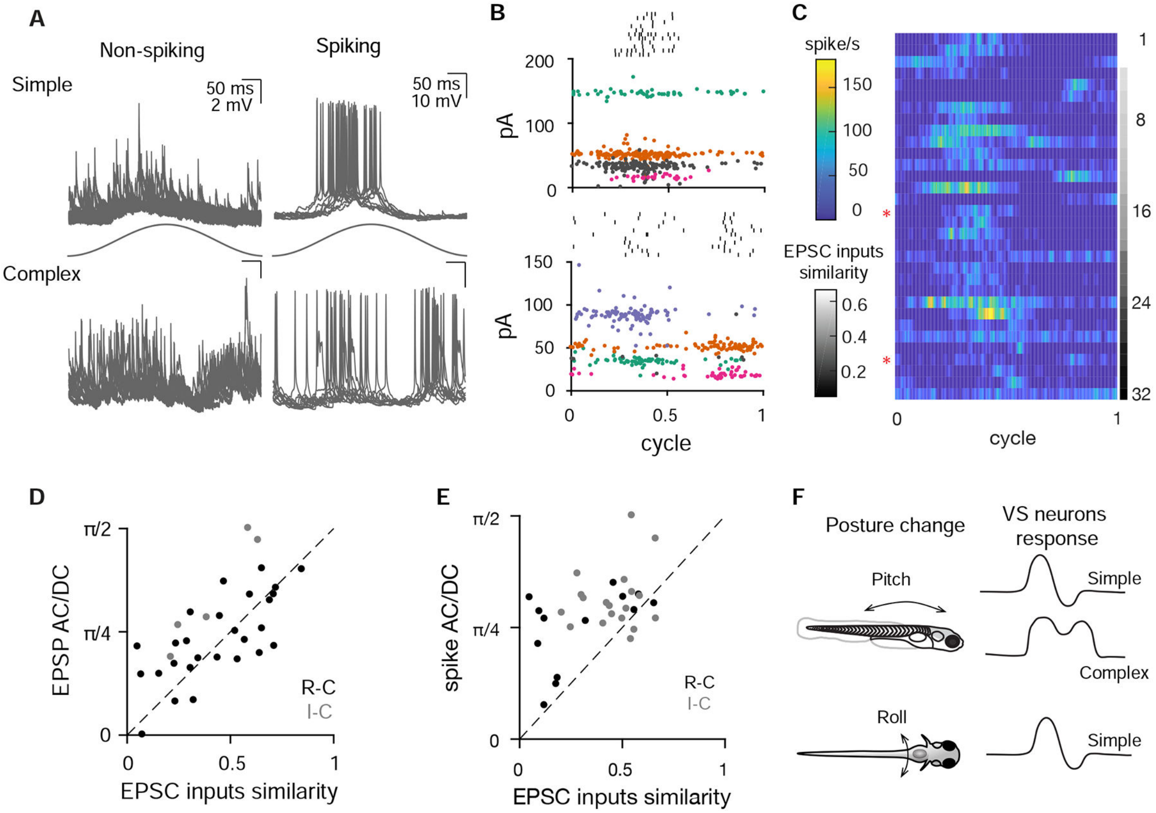

Figure 8:

Complex central tuning arises from divergent afferent inputs

A. Example subthreshold and spiking responses from VS neurons with simple tuning (top) or more complex, multi-phase responses (bottom) during 2 Hz, 0.02 g translational movement (11–12 cycles overlaid).

B. Example spiking cells (same as in A), showing that simple (top) and complex (bottom) spiking tuning response are constructed from afferent inputs with similar and different tuning directions, respectively. At top (black) is the sensory-evoked spike raster. Colored and gray dots represent sensory-evoked EPSCs; all the EPSCs with the same color in a panel are inferred to arise from the same afferent. Gray, EPSCs that are not necessarily from individual afferents, based on the absence of clear refractory period structure in autocorrelogram. EPSCs and rasters are from 11–12 cycles.

C. Average spiking rate of VS neurons during a cycle of sensory stimulation, ranked from more similar EPSC inputs to more different EPSC inputs, n=32. Red asterisks label the example spiking simple and complex VS neuron in A and B.

D. Correlation of EPSC inputs similarity index and EPSP AC/DC response ratio (see Methods), for all non-spiking VS neurons with multiple convergent afferents. Sensory tuning of afferent inputs and EPSPs was measured on the R-C axis (black, n=27) and I-C axis (grey, n=5). Dashed, unity line. R: 0.67, p=2.9e-5

E. Correlation of EPSC input similarity index and spike activity AC/DC ratio, for all spiking VS neurons on the R-C axis (black, n=13 recordings) and I-C axis (gray, n=19). Dashed, unity line. R: 0.48, p=5.5e-3.

F. Summary of different VS neuron responses to posture change on the pitch and roll axes.